Novel Electrolyte and Cathode formulation for Li-ICl Batteries

Daniele Congiu

October 12, 2023

Version: Final Draft

International Business Machines Corporation
Politecnico di Torino

Novel Electrolyte and Cathode formulation for Li-ICl Batteries

Daniele Congiu

1. Reviewer	Carlo Ricciardi Department of Applied Science and Technology Politecnico di Torino
Supervisors	Maxwell Giammona and Vidushi Sharma

October 12, 2023

Daniele Congiu
Novel Electrolyte and Cathode formulation for Li-ICl Batteries
October 12, 2023
Reviewers: Carlo Ricciardi
Supervisors: Maxwell Giammona and Vidushi Sharma

International Business Machines Corporation, Almaden Lab
Battery Group
Politecnico di Torino
650 Harry Road, 95120
San Jose

Contents

1 **Background** 3
- 1.1 Introduction to Li-ion batteries 4
- 1.2 Conversion battery systems 8
- 1.3 Next generation Li-Iodine batteries 10
  - 1.3.1 Anode 11
  - 1.3.2 Cathode 12
  - 1.3.3 Electrolyte 12
- 1.4 Motivation 14

2 **Experimental methodology** 15
- 2.1 Materials and Cell Construction 15
  - 2.1.1 Cell Evaluation 16
- 2.2 Measures and Analysis 16
  - 2.2.1 Galvanostatic Cycling with Potential Limitation 16

3 **Cathode Design and Optimization** 19
- 3.1 Binder effect 20
- 3.2 Comparison dissolution and integration 22
  - 3.2.1 Integration effect 23
  - 3.2.2 Diffusion-Limited Process 25

4 **Optimizing LiCl in Electrolyte** 27
- 4.1 Design of Experiment 27
  - 4.1.1 Salt and solvent concentration ranges 28
  - 4.1.2 Data Collection 29
  - 4.1.3 Machine Learning 33

5 **Conclusion** 41

6 **APPENDIX-A** 45
- 6.1 Training tests 45
- 6.2 Lithium chloride in electrolyte 47
- 6.3 Data collection 50

7 **APPENDIX-B** 55

7.1 Models comparison 55
7.2 HOT ENCODED TABLE 60

8 APPENDIX-C 67

8.1 Experimental measures of cathode optimization 67
8.2 Solvent amount comparison 68
8.3 PVP concentration comparison 69
8.4 PVP concentration comparison 70
8.5 PVP and MADQUAT comparison 71
8.6 Increased dosing percentage 72
8.7 Integration and dissolution collaboration 73

List of Figures

1.1 Global battery industry growth by application and region by 2030. Adopted and reprinted with authorization from [1] 4
1.2 Schematic representation of a Lithium-ion battery. Adapted and reprinted from [3]. 6
1.3 Lithium - Iodine Mono-Chloride battery cell scheme, charge process. . 11

3.1 Chemical structure of PVP-I (left) and MADQUAT (right). 20
3.2 Schematic depicting of the fabricating process of the polymer-modified I_2/Porous carbon composites. Adopted and reprinted form [11]. 21
3.3 Representations of Capacity (left) and Coulombic efficiency (right) . . 21
3.4 Direct comparison between integrated and dissolved systems. 24

4.1 Design of experiment, confrontation between a human and a machine approach. Adopted and reprinted from [15]. 28
4.2 Box representation of components distribution. The box in the middle of the plot represents the middle 50% of the data, often referred to as the interquartile range (IQR).The lines, or whiskers, extend from the box to the smallest and largest values within 1.5 times the IQR. The triangle represents the average value, the circles represent the outliers point. 31
4.3 Heatmaps for correlation between the 8 independent variables on the left the variable-capacity PC and on the right the variable-cycling life PC. 32
4.4 Pearson coefficient of $LiBOB$ concentration in molar percentage and capacity. 33
4.5 Fitting MSE performances of the shortlisted methods. 35
4.6 Fitting R^2 performance of the shortlisted methods. 35
4.7 Cross validation MSE performances of the shortlisted methods. 36
4.8 Cross validation R^2 performances of the shortlisted methods. 36
4.9 Performances of the tuned and untuned models. 37
4.10 Two variable correlation, with the capacity. Red dots represent the experimental points. 38

6.1 Results of the GCPL for the electrolytes design by the AI trained until January. (a-b-c-d) Experiment for 30% dosing. (e-f-g) Experiment at 50 %. 45

6.2 Results of the GCPL for the electrolytes design by the AI trained until January. (a-b-c) Experiment for 60% dosing. (d-e-f) Experiment at 70 %. 46

6.3 Results of the GCPL for the electrolytes design by the AI trained until March.(a-b) Experiment for 70 % dosing. 46

6.4 Results trying to substitute the solvent A. Experiment for 55% dosing.(a-b) Cells using solvent E, (c-d) cells using solvent F. 47

6.5 Capacity during the standard GCPL for three cells using solvent D. Experiment for 35% dosing. (a) Cycling life without rate test, (b-c) Standard test. 48

6.6 Nyquist plot of the electrolyte volumes comparison. (cell 1) 40 μl, (2) 60 μl, (3) 90 μl, (4) 110 μl 49

6.7 Capacity during the standard GCPL for 4 different volumes of electrolyte. Experiment for 50% dosing. (a) 40 μl, (b) 60 μl, (c) 90 μl, (d) 110 μl 49

6.8 Comparison between capacity $[mAh/g]$ of 5 different electrolytes composition at different charge/discharge rates. In Particular $0.5-1-2-3-4-5-10\ mA/cm^2$. Experiment for 40% dosing. There are 2 additional formulation used as reference. 50

7.1 Comparison between the predicted capacity and the measured for Linear regression. Fitting (Left) using all the points for training and the same points for testing. Cross Validation (Right) 5 fold, 4 of them used for the training and the last one for the testing. Are also reported the values of MSE (mean squared error) and R^2 55

7.2 Comparison between the predicted capacity and the measured for support vector regression with linear kernel. Fitting (Left) using all the points for training and the same points for testing. Cross Validation (Right) 5 fold, 4 of them used for the training and the last one for the testing. Are also reported the values of MSE and R^2 56

7.3 Comparison between the predicted capacity and the measured for support vector regression with Radial basis function kernel. Fitting (Left) using all the points for training and the same points for testing. Cross Validation (Right) 5 fold, 4 of them used for the training and the last one for the testing. Are also reported the values of MSE and R^2 56

7.4 Comparison between the predicted capacity and the measured for support vector regression with Sigmoid kernel. Fitting (Left) using all the points for training and the same points for testing. Cross Validation (Right) 5 fold, 4 of them used for the training and the last one for the testing. Are also reported the values of MSE and R^2 57

7.5 Comparison between the predicted capacity and the measured for support vector regression with Polynomial kernel with 5 degree of freedom. Fitting (Left) using all the points for training and the same points for testing. Cross Validation (Right) 5 fold, 4 of them used for the training and the last one for the testing. Are also reported the values of MSE and R^2 57

7.6 Comparison between the predicted capacity and the measured for support vector regression with Polynomial kernel with 8 degree of freedom. Fitting (Left) using all the points for training and the same points for testing. Cross Validation (Right) 5 fold, 4 of them used for the training and the last one for the testing. Are also reported the values of MSE and R^2 58

7.7 Comparison between the predicted capacity and the measured for support vector regression with Polynomial kernel with 10 degree of freedom. Fitting (Left) using all the points for training and the same points for testing. Cross Validation (Right) 5 fold, 4 of them used for the training and the last one for the testing. Are also reported the values of MSE and R^2 58

7.8 Comparison between the predicted capacity and the measured for support vector regression with Polynomial kernel with 15 degree of freedom. Fitting (Left) using all the points for training and the same points for testing. Cross Validation (Right) 5 fold, 4 of them used for the training and the last one for the testing. Are also reported the values of MSE and R^2 59

7.9 Comparison between the predicted capacity and the measured for Random forest regressor. Fitting (Left) using all the points for training and the same points for testing. Cross Validation (Right) 5 fold, 4 of them used for the training and the last one for the testing. Are also reported the values of MSE and R^2 59

7.10 Comparison between the predicted capacity and the measured for Gaussian regression with exponential kernel. Fitting (Left) using all the points for training and the same points for testing. Cross Validation (Right) 5 fold, 4 of them used for the training and the last one for the testing. Are also reported the values of MSE and R^2 60

7.11 Comparison between the predicted capacity and the measured for Gaussian regression with Matern32 kernel. Fitting (Left) using all the points for training and the same points for testing. Cross Validation (Right) 5 fold, 4 of them used for the training and the last one for the testing. Are also reported the values of MSE and R^2 60

8.1 (a)-(b) Capacity during the standard cycle for the first dosing solution (c)-(d) Capacity during the standard cycle for the second solution (e)-(f) Capacity during the standard cycle for the third solution. Experiment for 40% dosing. 67
8.2 Comparison varying the quantity of solvent EtOH, (c-d) have double solvent quantity with respect to (a-b). Increase in the efficiency 68
8.3 Comparison varying the amount of binder, (a-b) low quantity of PVP, and target dosing 45%. (c-d) doubled quantity of PVP with respect of (a-b), (c) target dosing 45%, (d) target dosing 60%. (e) same quantity of (c-d) with increased KB and LiCl, (e) target dosing 45%. (f) doubled quantity of PVP with respect of (c-d), (f) target dosing 45% 69
8.4 Comparison varying the amount of binder, with 60% target dosing. (a-b) no PVP binder. (c-d) 4 mg of PVP binder. (e-f) 8 mg of PVP binder. (g-h) 16 mg of PVP binder. 70
8.5 Comparison varying the amount of binder, with 60% target dosing. (a) PVP binder.(b) PVP and MADQUAT (1:1 wt.) binder.(c) MADQUAT binder.(d) no binder. 71
8.6 (a-b) target 60% dosing.(c) target 60% dosing, with increased LiCl. (d-e) target 70% dosing. 72
8.7 Comparison between LiCl just in the cathode or both in cathode and electrolyte, target dosing 60%. (a-b-c-d-e-f-g) no binder, (h-i) PVP and KB. (a-b-h-i) no LiCl in the electrolyte, (c-d) no LiCl in the electrolyte, with slightly different compositions. (e-f) LiCl in the electrolyte. (g) LiCl in the electrolyte, with slightly different compositions. 73

Acknowledgement

I would like to thank my university for the opportunity to work with IBM Research. I want to express my gratitude to IBM, and in particular, the Battery Group, for welcoming me and providing their support. Special thanks go to Max Giammona and Vidushi Sharma for their kindness and expertise in assisting me. I am grateful to Murtaza Zohair for his unwavering availability and help in my understanding, always with a friendly demeanor. Andy T. Tek, the superhero of the Battery Lab, deserves thanks for being ever available in times of need. Khanh Nguyen and Phill Medina, thank you for all the laughter and companionship during the long days in the lab. Antony Fong, for his constant companionship and sunny disposition, and of course, for renting us the house. Lastly, I would like to thank Young Hey Na for her leadership and willingness to help with all needs, always with a smile.

I would also like to express my gratitude to my family and friends for their support throughout my entire academic journey, starting with my mates in countless adventures (I won't list you all), including the Musketeers, and a special thanks to my roomates in San Jose.

1

Background

The need for a strong and effective contrast to climate change and pollution is broadly recognized. The battery value chain is one of the major near-term drivers to realize the 2°C Paris Agreement goal in the transport and power sectors. Indeed, batteries can help convert the vehicle market to electric and are needed for a wide application of renewable energy sources optimizing energy production. According to [1], batteries could enable 30% of the required reductions in carbon emissions in the transport and power sectors, provide access to electricity to 600 million people who currently have no access, and create 10 million safe and sustainable jobs around the world.

Global battery demand is expected to grow by 25% annually to reach 2,600 GWh in 2030. Batteries play an increasingly important role in three areas:

1. Decarbonizing transport through electrification;

2. Enabling the shift from fossil fuel to renewable power generation as a dispatchable source of electricity;

3. Helping to provide access to electricity to off-grid communities.

This means batteries can fundamentally reduce Green House Gas emissions in the transport and power sectors, which currently comprise roughly 40% of global GHG emissions, and contribute to the United Nations Sustainable Development Goals.

Between 2010 and 2018, there was a 30% annual growth in battery demand, culminating in a volume of 180 GWh by 2018. Under the baseline scenario, it is anticipated that the market will continue to expand at an estimated annual rate of 25%, ultimately reaching a volume of 2,600 GWh by 2030. The primary drivers behind this increasing demand are the electrification of the transportation sector and the utilization of batteries within electrical grids (refer to Figure 1.1 for a visual representation). By the year 2030, passenger cars are expected to constitute the largest portion of global battery demand, accounting for 60%, followed by the commercial vehicle segment at 23%. In terms of geographical distribution, China stands out as the largest market, representing 43% of the total. Consumer electronics,

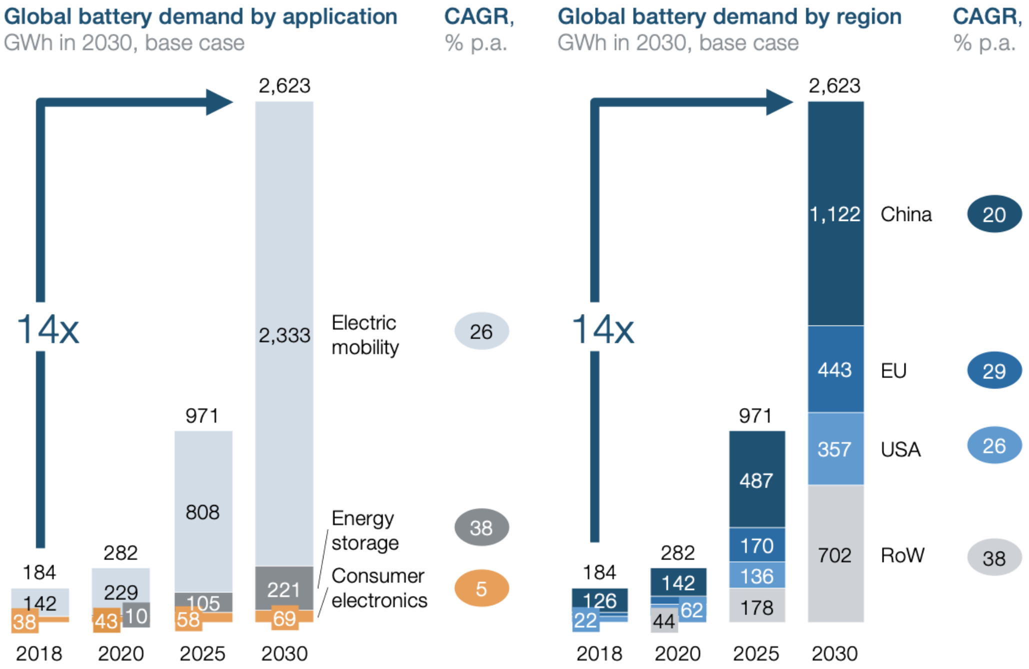

Figure 1.1: Global battery industry growth by application and region by 2030. Adopted and reprinted with authorization from [1]

which currently contribute more than 20% to the market, are projected to hold only a minor share in the global battery market by 2030.

In the pursuit of enhancing battery technology, several critical challenges must be addressed to achieve greater efficiency, prolonged cycling life, enhanced total capacity, and accelerated charging rates. These imperatives underscore the significance of ongoing research and innovation in the realm of battery development. As the demand for energy storage solutions intensifies within diverse industries, addressing these challenges becomes paramount to unlocking the full potential of battery systems and advancing the energy landscape towards a more sustainable future.

1.1 Introduction to Li-ion batteries

In recent years, there has been significant research on new and innovative energy storage technologies driven by the increasing demand for portable electronic devices, electric vehicles, and the need for optimal solutions. The need for large quantities of batteries, combined with the requirement for miniaturized and high-efficiency devices, has spurred research into new technologies.

Among the main energy storage devices, Li-ion batteries seem currently the most viable solution. The main alternatives, such as supercapacitors and fuel cells, are not optimal due to the low energy density of supercapacitors [2] and safety issues associated with both.

The research around rechargeable batteries was born in the 1960s, chemists in Europe were exploring the chemistry of reversible insertion of lithium into layered transition-metal sulfides. Further research bring to the light a new revolutionary technology, that valued the Nobel Prize in Chemistry in 2019 to Akira Yoshino alongside M. Stanley Whittingham and John B. Goodenough [3].

Li-ion batteries in general are composed of two electrodes, each of which is made of a material able to form a RedOx couple. One of the two is designed to be easy to oxidize, and the other to be reduced, Figure 1.2; each of the two half-reactions is correlated with a standard potential with respect to a reference. To have a spontaneous reaction the Gibbs free energy has to be lower than 0 ($\Delta G < 0$), the relation between the reduction potential and the Gibbs free energy is shown in the equation 1.2. The difference between the two potentials is the open circuit voltage of the cell, Equation 1.1.

The two electrodes are called anode (negative during discharge) and cathode (positive during discharge), between them there is an electrolyte that allows ions to move from one electrode to the other, insulating the electrons. To avoid short circuit the two electrodes are physically separated by a separator, that has to be permeable to the ions.

$$\Delta E_{cell} = \Delta E_{red} - \Delta E_{ox} \tag{1.1}$$

When we close the circuit, the current starts to flow, and the reaction proceeds. The reduction potential changes following the Nernst equation 1.3. When the circuit is closed, allowing current to flow, the electrode potentials change according to the Nernst equation 1.3, which accounts for non-standard conditions. The Nernst equation relates the electrode potential (E_{red}) to the standard potential, temperature (T), the Faraday constant (F), the charge number (z), and the concentrations of the oxidized ($[Ox]$) and reduced ($[Red]$) species:

$$\Delta E_{red} = -\frac{\Delta G}{zF} \tag{1.2}$$

$$\Delta E_{red} = \Delta E^0_{red} + \frac{RT}{zF} \ln\left(\frac{[Ox]}{[Red]}\right) \tag{1.3}$$

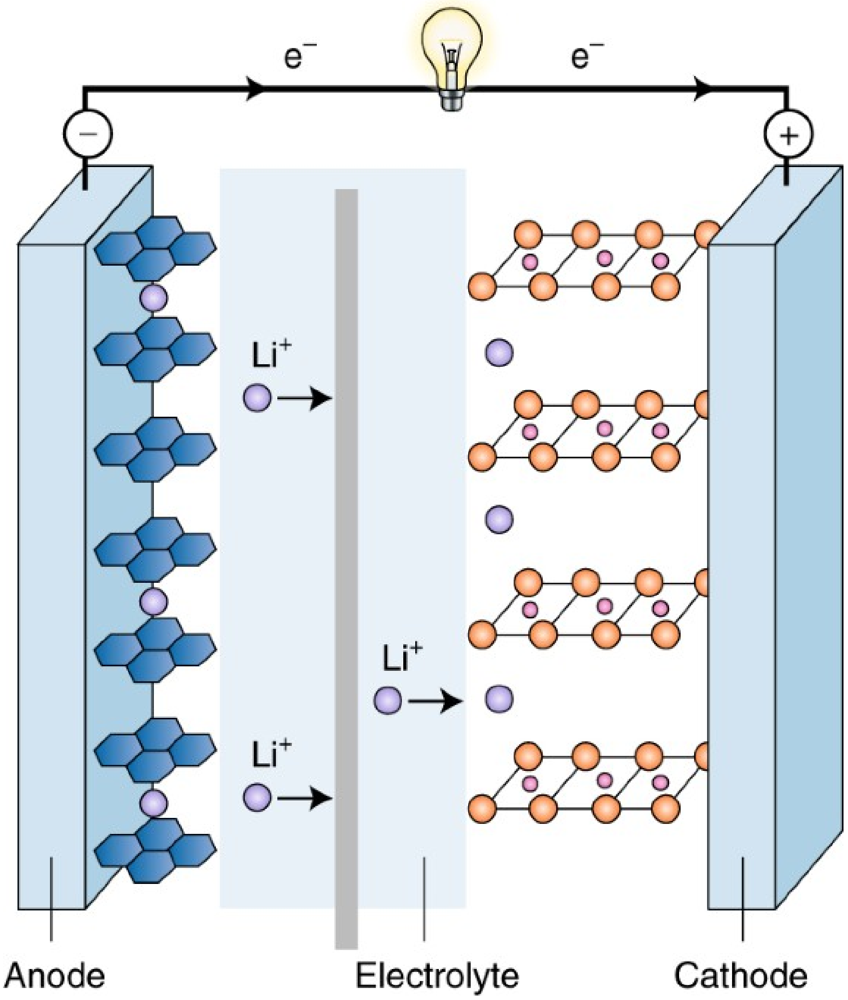

Figure 1.2: Schematic representation of a Lithium-ion battery. Adapted and reprinted from [3].

Overall, a battery's function hinges on the interplay of these electrode reactions. As the battery discharges, the anode undergoes oxidation, releasing electrons that flow through the external circuit to the cathode. At the cathode, reduction reactions occur, consuming the electrons and balancing the charge transfer. This cyclic process allows batteries to store and release electrical energy, enabling them to power a wide range of applications.

Currently used Lithium-ion batteries are based on intercalation technology. Intercalation electrodes are a class of materials commonly used in rechargeable batteries, especially lithium-ion batteries. These electrodes work by allowing ions, typically lithium ions, to be inserted and extracted reversibly into the crystal structure of the electrode material during charge and discharge cycles. This process is often referred to as intercalation or intercalation/de-intercalation. The host material has layered or open-framework structures that can accommodate the insertion of guest ions between their layers or into their structures without causing significant structural changes. During charging, lithium ions are extracted from the intercalation host, creating a potential difference. During discharge, lithium ions are inserted back into the host material. The process is highly reversible, contributing to the stability and longevity of intercalation-based batteries. Common intercalation electrode materials include graphite for the anode in lithium-ion batteries and transition metal oxides or sulfides for the cathode. Intercalation electrodes offer advantages like high energy density, good cycle life, and relatively stable performance a brief summary of the performances is reported in Table 1.1.

Table 1.1: Characteristics of representative intercalation cathode compounds; crystal structure, theoretical/experimental/commercial gravimetric and volumetric capacities, average potentials, and level of development. Adapted and reprinted from [4].

Crystal structure	Compound	Specific capacity (mAh g^{-1}) (theoretical/experimental/typical)	Volumetric capacity (mAh cm^{-3}) (theoretical/typical)	Average voltage (V)	Level of development
Layered	$LiTiS_2$	225/210	697	1.9	Commercialized
	$LiCoO_2$	274/148/145	1363/550	3.8	Commercialized
	$LiNiO_2$	275/150	1280	3.8	Research
	$LiMnO_2$	285/140	1148	3.3	Research
	$LiNi_{0.33}Mn_{0.33}Co_{0.33}O_2$	280/160/170	1333/600	3.7	Commercialized
	$LiNi_{0.8}Co_{0.15}Al_{0.05}O_2$	279/199/200	1284/700	3.7	Commercialized
	Li_2MnO_3	458/180	1708	3.8	Research
Spinel	$LiMn_2O_4$	148/120	596	4.1	Commercialized
	$LiCo_2O_4$	142/84	704	4.0	Research
Olivine	$LiFePO_4$	170/165	589	3.4	Commercialized
	$LiMnPO_4$	171/168	567	3.8	Research
	$LiCoPO_4$	167/125	510	4.2	Research
Tavorite	$LiFeSO_4F$	151/120	487	3.7	Research
	$LiVPO_4F$	156/129	484		

While Li-ion batteries have revolutionized portable electronics and electric vehicles, there are limitations that researchers aim to address. These limitations include concerns about energy density, charging time, and safety. Energy density improvements are crucial for extending battery life and enhancing device performance. Additionally, faster charging solutions are sought after to minimize downtime and improve user convenience. Lastly, safety concerns related to overheating and fire risks motivate researchers to explore new chemistries that offer enhanced stability. As a result, the research community is dedicated to developing batteries with higher energy densities, shorter charging times, and improved safety profiles to meet the evolving demands of modern technology.

1.2 Conversion battery systems

Battery systems' electrodes can be categorized into intercalation and conversion modes [5]. Currently, commercial batteries use intercalation methods, which are highly stable in cycling and reduce self-discharge, but they partially sacrifice energy density. On the other hand, the conversion-type [6] is not yet a viable solution for commercial applications but appears to be a promising approach to increase capacity and the working rate of current technology. This is because they allow for the activation of more electrons in each redox process.

Unlike intercalation, conversion involves chemical reactions that cause the electrode material to change its composition during charge and discharge cycles. In conversion electrodes, the material undergoes reversible conversion reactions, where the active species in the electrode material react with ions from the electrolyte to form new compounds. During discharge, the cathode material is reduced, incorporating ions from the electrolyte into its structure. During charging, the reverse process occurs, and the material is oxidized back to its initial state. Conversion electrodes can offer high capacity due to the more significant change in composition compared to intercalation electrodes, the reaction usually involves one or more electrons each. However, they often suffer from challenges related to volume changes, phase transitions, and mechanical stress during cycling.

For example S, MoS_2 and I_2 batteries are widely explored system in the conversion electrode direction.

Sulfur is one of the most abundant elements on earth and it is an electrochemically active material that can accept up to two electrons per atom at $\sim 2.1\,V\,vs\,Li/Li^+$. As a result, sulfur cathode materials have a high theoretical capacity of $\sim 1675\,mAhg^{-1}$, and lithium-sulfur (Li-S) batteries have a theoretical energy density of $\sim 2600\,Whkg^{-1}$ [7].

Molybdenum disulfide (MoS_2) is another promising candidate for conversion-type batteries due to its unique properties. MoS_2 undergoes reversible chemical reactions during charge and discharge cycles, leading to changes in its composition. This conversion process allows for the activation of multiple electrons in each redox reaction, potentially providing higher capacity compared to intercalation-based batteries. The theoretical capacity of MoS_2 as an active material for conversion batteries has been studied extensively, with reported values ranging from approximately 650 mAh/g to 1000 mAh/g [8, 9]. These investigations highlight MoS_2's potential to achieve substantial energy storage capabilities, making it a subject of ongoing research in the field of advanced battery materials.

Li-Iodine batteries are also a great option among rechargeable conversion batteries and their popularity can be attributed to the following factors:

- High theoretical capacity and good operating voltage;
- Good compatibility with electrolytes;
- Low cost and abundance of materials;
- High rate capability.

Rate capability is going to be a crucial element in the next generation of commercial batteries, in line with the guidelines provided by the US battery consortium, which require a high charge rate capable of charging 80% of the state of charge in 15 minutes for electric vehicle applications. This aspect bodes well for the future potential of conversion batteries. The conversion is based on the following reactions, equation 1.4 and 1.5.

$$2Li \rightarrow 2Li^{+} + 2e^{-} \qquad E_{ox} = -3.04V \tag{1.4}$$

$$2I^{+} + 2e^{-} \rightarrow I_2 \qquad E_{red} = -0.54V \tag{1.5}$$

Conversion electrodes hold significant promise for high-capacity rechargeable batteries, but they also present a wide range of challenges to overcome. One of the main difficulties lies in accommodating the significant volume expansion that occur during the conversion reactions. This volume changes can lead to mechanical stress, destruction of the electrode material, and electrode degradation over multiple charge-discharge cycles. Additionally, conversion reactions often involve complex phase transitions, leading to reversible and irreversible structural changes that can affect the battery's performance and cycle life. Another challenge is managing side reactions that can occur between the electrode material and the electrolyte, leading to capacity fading and reduced efficiency. Researchers are actively working on addressing these challenges through innovative electrode design, nanostructuring techniques, and electrolyte optimization to unlock the full potential of conversion-based batteries for practical applications.

In addition the shuttling is a major issue with I_2 and S, shuttling refers to the migration of active material from an electrode to the other. The active material leaves the electrode and react with other components of the battery inducing capacity fading and poor cycle life. The design of the electrolyte is crucial, indeed the solubility of the species containing active material is a major issue. Together with the electrolyte also the cathode can be design to physically or chemically trap the active species avoiding the dissolution and the consequent side reaction[10, 11].

Another possible approach can be the design of a complex separator able to filter the migration of ions, avoiding to the active material to travel form the cathode to the anode. The challenges of this approach relies in finding a separator with extremely high efficiency that select correctly the ion without slowing down the reaction and diffusion.

1.3 Next generation Li-Iodine batteries

Focusing on the possibles developments of the Li-Iodine technology, Xianliang Li et al. [12] unlocked the "second electron" making the second step possible by including $LiCl$ in the electrolyte. Iodine has three main possible oxidation states exploitable, $I^-/I^0/I^+$, and the two characteristic reactions are reported below in Equations 1.3 and 1.3.

First step

$$I^- \leftrightarrow I^0 + e^- \quad (0.54\,Vvs : SHE)$$

Second step

$$I^0 \leftrightarrow I^+ + e^- \quad (0.99\,Vvs : SHE)$$

The I^- is usually obtained from LiI. Instead, to stabilize I^+, it is necessary to introduce very electronegative ions. This can almost double the theoretical capacity. Iodine also has further oxidation states that currently seem impossible to exploit. $LiCl$ has a great effect on the stabilization of I^+ ions. Unfortunately, $LiCl$ is not highly soluble in the classic electrolyte solvents, introducing to the research for new solvents. Moreover, if it is included in the electrolyte, it seems to have a detrimental effect on the solid electrolyte inter-phase (SEI) layer, increasing the shuttling. In addition to this, one of the goals for the optimization of the $Li - I_2$ batteries is to increase the mass of LiI, and along with it, the quantity of $LiCl$ has to increase to maintain the molar ratio constant, in order to allow a complete reaction. Thus we will need to dissolve even higher amount of $LiCl$ requiring specific solvents.

A possible alternative could be to include $LiCl$ in the cathode, which leads to issues related to binding it and LiI to the carbon coat. Increasing just the amount of LiI included in the cathode is already challenging, and increasing the amount of both LiI and $LiCl$ will require a lot of effort.

Cathode

$$I^- - e^- \rightarrow I^0$$

$$I^0 - e^- + Cl^- \rightarrow I^+Cl^-$$

Anode

$$2Li^+ + 2e^- \rightarrow 2Li$$

Figure 1.3, is a schematic representation of a Lithium (Anode) - Iodine mono-Chloride (Cathode), during the charge process. In the following sections all the components of the unit cell are analyzed.

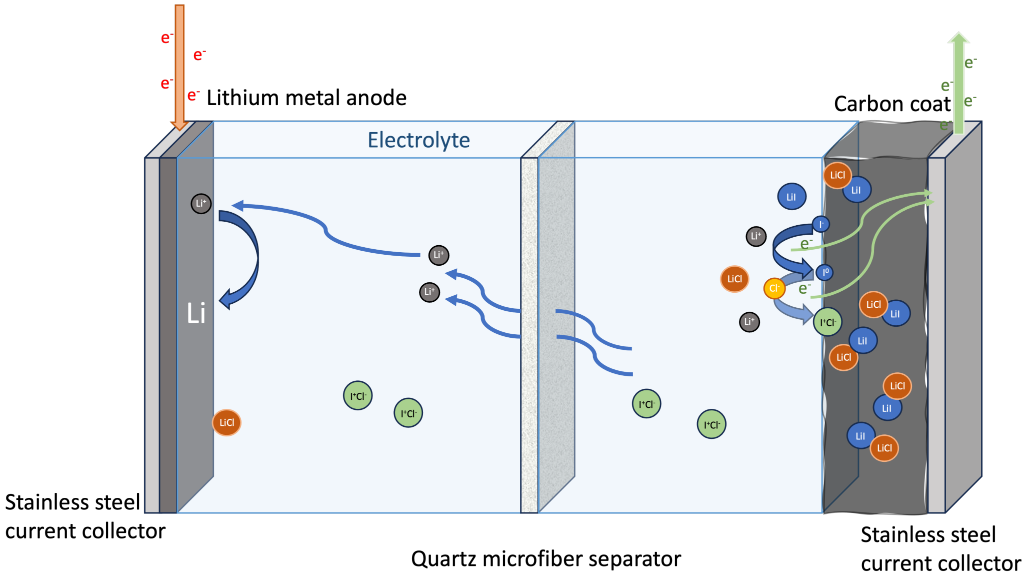

Figure 1.3: Lithium - Iodine Mono-Chloride battery cell scheme, charge process.

1.3.1 Anode

The anode in a conversion system has to undergo a chemical reaction, reversibly. In our system, we use a metal lithium anode able to provide a huge amount of capacity, equation 1.4.

Usually, the lithium anode can cause the formation of dendrites due to the non-homogeneous growth of lithium. However, the system we are exploiting does not form dendrites. This is in particular due to the high stability of the solid electrolyte interphase (SEI) layer and the good mobility of ions that allows a well spread growth of the lithium.

Furthermore, Lithium-Iodine batteries have issues due to shuttling, so the formation of a robust SEI layer is fundamental to obtaining high performances. The oxygen gas has been found, by Giammona et al. [13], as one possible solution, making the cells easier to assembly and forming nitrate(Li_3N) and iodate($LiIO_3$) makes the SEI more robust, suppressing dendritic growth and mitigating the effect of shuttling, together with the presence of $LiNO_3$ and $LiBOB$ in the electrolyte. The cells that use this technology are usually named Oxygen assisted Lithium-Iodine battery (OALI) and had demonstrated superior performance with much less technology requirement and cheaper production.

1.3.2 Cathode

The cathode reaction of a $Li - I_2$ is reported in equation 1.5 characterized by the high resistance of the iodine that cause a sluggish reaction, combining conductive network and iodine species boosts interior charge transfer, leading to a better rate performances.

Typically, iodine is adsorbed on a host material, such as a carbon coat, to enhance conductivity. Carbon materials are the most commonly used host for rechargeable iodine batteries (RIBs),owing their porous structure, high conductivity and low cost. However, constructing an efficient cathode presents a challenge. It is particularly difficult to achieve a high quantity of iodine in the carbon without causing cathode dissolution during cycling. The dissolution of active material in this kind of systems is usually the main cause of shuttling, and thus of performances vanishing. By creating chemically and physically sophisticated structures combined with a stable solid electrolyte interphase (SEI) layer, it becomes possible to achieve dosing of over 60% by weight. Also combining $polymer - I_2$ complex can help maintaining the high rate capacity stabilizing the cycling life[14].

1.3.3 Electrolyte

The electrolyte has to be carefully designed, the solubility of the iodine species may cause shuttling causing self discharge and anode passivation. For a suitable electrolyte, the following requirements have to be satisfied:

- A wide electrochemical window to avoid side reactions of the electrolyte;
- Moderate interaction between solvent molecules and ions;
- Avoid side reactions with the electrodes or with any intermediates;
- Electron-insulator and ion-conductor.

All these considerations make up the "electrolyte tetrahedron" and all the conditions have to be considered. To obtain all the requirements, the electrolytes we use include $LiTFSI$, $LiNO_3$, $LiBOB$, $LiCl$, DOL, DMI, EC, and $TEGDME$. Each of these components plays a distinct role in the overall battery system.

The salts, such as $LiTFSI$ (Lithium bis(trifluoromethanesulfonyl)imide), $LiNO_3$ (Lithium nitrate), $LiBOB$ (Lithium bis(oxalato)borate), and $LiCl$ (Lithium chloride), contribute to the ionic conductivity of the electrolyte. They provide the necessary lithium ions for the electrochemical reactions, and their selection can significantly impact the stability and performance of the battery. For instance, the choice of salts can affect the solubility and stability of the cathode and anode materials, the formation of the solid electrolyte interphase (SEI) layer. The $LiNO_3$ has the effect of improving the coulombic efficiency and help with the shuttling forming a robust SEI layer.

The solvents, including DOL (1,3-Dioxolane), DMI (Dimethyl isophthalate), EC (Ethylene carbonate), and $TEGDME$ (Tetraethylene glycol dimethyl ether), are responsible for dissolving the salts and creating a conductive medium for lithium ions to move between the anode and cathode. Solvent selection is crucial for achieving the desired properties of the electrolyte, such as high ionic conductivity, low viscosity, wide electrochemical stability window, and good compatibility with the electrode materials. Different solvents have varying abilities to solvate the lithium ions and form a stable SEI layer on the electrode surfaces, which impacts the battery's overall performance, safety, and cycle life.

In summary, the careful combination of salts and solvents in the electrolyte is essential to achieve the desired electrochemical performance, stability, and safety of the conversion battery system. Each component's unique properties and interactions contribute to the overall behavior of the battery, making electrolyte design a critical aspect of advancing energy storage technologies.

In addition to all this consideration for our system extreme care was used in order to minimize the solubility of the iodine species.

1.4 Motivation

In the future, achieving higher capacity, rapid charging, and extended cycle life in batteries will be of major importance. The energy market is growing in an impressive way and it will not stop in a mid/long term view. Lithium-Iodine batteries have potential to become a Next-Gen commercial technology thanks to their stability, high rate capability and low costs, but in order to achieve this the second step has to be stably unlocked. In this study, we investigate and analyze the optimization of the electrolyte and cathode as distinct problems.

The cathode design is a complex task due to the sophisticated structure and the high solubility of active materials. We propose a design able to integrate all the active material onto the cathode, allowing the exploitation of two different oxidation states of iodine, outperforming the our current technology at high rates.

The optimization of the electrolyte for these types of batteries is also complex due to the numerous variables involved. It presents an excellent opportunity to leverage machine learning algorithms for formulation design. In general the discovery of "high entropy" materials can be accelerated by Artificial Intelligence.

2

Experimental methodology

2.1 Materials and Cell Construction

In this work, I used 2032 type coin cells sealed under either an argon or clean, dry air atmosphere.

To fabricate the cathodes, a slurry of high surface area activated carbon (MSC-30SS, Kandsai Coke), a high conductivity carbon additive (Ketjen Black (KB), EC600JD, Lion Chemical), and either styrene-butadiene rubber (SBR, PSBR100, Targray) and carboxymethylcellulose Sodium Salt (CMC, low viscosity, Sigma Aldrich) in water or PTFE in alcohol as the binder and base solvent, respectively, was prepared. Slurries were prepared at between 10-20% solids by weight and spread coated onto either carbon cloth (Panex PW06, Fuel Cell Store) or stainless-steel foil (10 um thickness, SS304). Electrode sheets were coated and dried under ambient conditions with approximate final compositions of 76.5/8.5/13/2 MSC-30SS/KB/SBR/CMC or 83.5/16.5 KB/PTFE. Carbon electrodes were punched into 11 mm ø disks and transferred into an argon glovebox where they are stored on a hotplate at 120 °C until used. Undosed carbon electrodes had an approximate mass loading of 4-6 mg/cm^2 and a thickness of 200 – 300 μm. To prepare lithium-iodide electrodes, carbon disks were individually weighed and dosed, under an argon atmosphere, to either 40% or 60% loading lithium iodide (approx. 5 and 10 mg/cm^2 areal loading) by weight by sequential addition of lithium iodide from a 150-200 mg/ml solution in ethanol and then dried at 150 °C for at least 3 hours. Dosed cathodes were then stored at 150 °C until used.

The electrolytes comprised lithium bis(trifluoromethyl) sulfonylimide ($LiTFSI$, BASF) and lithium nitrate ($LiNO_3$, Sigma Aldrich) in a mixed solvent containing a certain ratio solvents in the total amount 100 μL of electrolyte was used in all cells that included a QMA separator and 60 μL for the CG2325 separator. All salts were dried at 150 °C for at least 24 hours under an argon atmosphere prior to use. All solvents were dried over 3Å molecular sieves, under an argon atmosphere for at least 24 hours prior to use.

Lithium metal (Honjo Metals, 250 μm thickness) anodes were punched to 13 mm ø for 2325 type coin cells. The Anode was usually polished in air, which should increase the robustness of the SEI. A Polypropylene/Polyethylene/Polypropylene trilayer membrane (Celgard 2325) was used as the separator, with separators being punched into 16 mm disks for the 2325 type coin cells. Also, as a separator, the QMA Whatman® QM-A quartz filters were often used, being punched into 16 mm disks for the 2325 type cells.

2.1.1 Cell Evaluation

All electrochemical measurements, including galvanostatic charge and discharge, cyclic voltammetry (CV), and electrochemical impedance spectroscopy (EIS), were conducted using EC-Lab® software and a multi-channel potentiostat (BioLogic, VMP3). All potentials are referenced against Li/Li+. To establish a more uniform starting condition, as well as to facilitate the formation of the enhanced OALI SEI layer, cells were first "conditioned" by cycling for 10 cycles at a rate of $0.5\ mA/cm^2$ before moving on to a cycling test at $1\ mA/cm^2$ or a rate test at a variable current density. Voltage cut-offs were set as 2.0V to 3.6V for cells with a stainless steel current collector and 2.75V – 3.6V for cells with a carbon cloth current collector.

2.2 Measures and Analysis

2.2.1 Galvanostatic Cycling with Potential Limitation

GCPL (Galvanostatic Cycling with Potential Limitation) is an electrochemical testing technique used to evaluate the performance and behavior of batteries or energy storage systems.

In GCPL, the battery or cell undergoes galvanostatic cycling, where a constant current is applied during charge and discharge processes. However, unlike traditional galvanostatic cycling, GCPL incorporates an additional potential limitation.

The potential limitation is introduced by imposing a voltage limit on the battery during cycling. This means that once the battery reaches a specific voltage threshold, the current is adjusted to maintain that voltage instead of allowing it to exceed or drop below the limit. This ensures that the battery operates within a predefined voltage range and avoids reaching extreme or potentially damaging voltages. In my setup, the voltage window was between 2 and 3.7 V, allowing for the reaction of iodine.

By incorporating potential limitation, GCPL provides several advantages. It helps control the battery's voltage and prevents overcharging or over-discharging, which can cause performance degradation or safety issues. It also allows for the examination of the battery's behavior and performance under specific voltage conditions, mimicking real-world scenarios more accurately.

GCPL is commonly used in battery research and development to study the capacity, efficiency, cycling stability, and degradation mechanisms of battery systems. It provides valuable insights into the electrochemical behavior and performance of batteries under controlled voltage conditions.

Formation cycles

All the routine starts with a PEIS, after 5 minutes of rest we start performing the formation cycles. In our setup, GCPL was set to run 10 formation cycles with a current of $0.5\ mA/cm^2$, in a voltage window between 2.1-3.7 V. These cycles are needed for the formation of a robust SEI (Solid Electrolyte Interface) and for the stabilization of the cell.

Rate Test

The second step is the rate test, where we test the cells at 7 different rates of charge and discharge, specifically with currents of $0.5 - 1 - 2 - 3 - 4 - 5 - 10\ mA/cm^2$ applied, in a voltage window between 2-3.8 V. Each rate runs for 5 cycles, followed by a 10-second rest period.

Cycling test

After the rate capability test, the cells undergo a cycling test. In this final section of our standard test, the cells are charged and discharged until the total capacity drops below 80% of the initial capacity. The current imposed on the cell is $1\ mA/cm^2$, in a voltage window between 2-3.8 V. This analysis provides insights into the cycling life of the cell.

3

Cathode Design and Optimization

After conducting a limited set of experiments focused solely on the dissolution of $LiCl$ in the electrolyte, it became apparent that addressing the shuttling problem through this approach posed significant challenges, and the results did not provide a clear direction for improvement. Consequently, a novel idea emerged: directly integrating $LiCl$ into the cathode, along with the use of a binder, can facilitate the formation of a complex structure to mitigate the shuttling issue. The literature suggests that PVP (polyvinylpyrrolidone) is an optimal choice for the binder, a material already employed in commercial applications [11]. However, the inclusion of the binder increases the cathode's resistance. We addressed this issue by introducing Ketjen Black to the complex cathode. The presence of two salts leads to a lack of uniqueness in the dosing percentage. Consequently, the ratio of the summed masses of LiI and $LiCl$ to the total cathode mass is reported as the dosing percentage.

Numerous experiments have been conducted, and their outcomes are detailed in Appendix-C.

To effectively localize $LiCl$ near LiI, the objective is to deposit it on top of the cathode. As discussed earlier, the cathode plays a pivotal role in the cell's operation. Integrating LiI within the carbon-coated matrix to form a composite cathode minimizes resistance and enables high-rate performance.

Among the significant challenges to address, briefly discussed in the introduction, the main one is the high solubility of polar iodide compounds in the electrolyte during cycling, leading to undesired side reactions that diminish battery performance. This challenge becomes even more pronounced with the additional presence of $LiCl$. To ensure effective integration into the cathode, it is imperative that chloride compounds remain within the cathode. An initial approach was to employ polymers to physically and chemically enhance the cathode's capability to trap both salts simultaneously.

Creating chemical interactions between PVP and iodine species can enhance stability by limiting the sublimation and dissolution of iodine. However, the current performance peaks with low iodine content (10% wt.)[11]. Binders may also pose challenges by reducing molecular mobility and hindering diffusion, thus affecting performance at high rates.

We initiated testing on possible binders, with PVP being the most common choice for iodine and already commercially utilized in iodine batteries. In parallel, we explored the prospective of MADQUAT (Poly(2-dimethylamino)ethyl methacrylate) methyl chloride quaternary salt) as a viable option for integrating $LiCl$.

3.1 Binder effect

As mentioned in the introduction, iodine is characterized by extremely high volatility. PVP demonstrates good properties and the capability to bind poly-iodides, which are typically the primary cause of shuttling.

PVP is widely recognized for its ability to bind with poly-iodides, especially I_3^-, as shown in Figure 3.1. Similarly, MADQUAT stabilizes the system with Cl^- ions, and we hypothesize that it could have a positive effect by retaining chloride within the cathode.

To address issues related to the cathode's conductivity, we also introduce Ketjen Black.

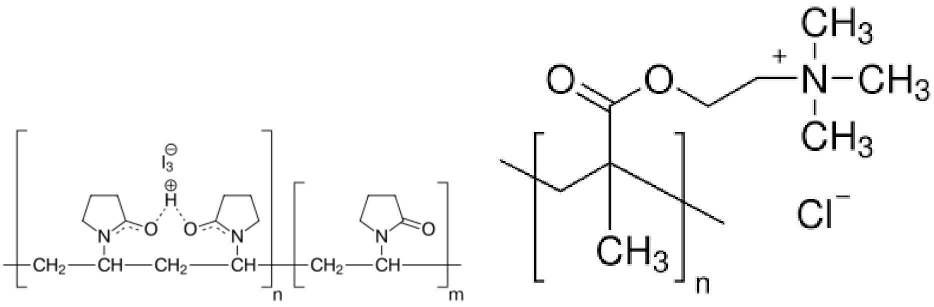

(a)

(b)

Figure 3.1: Chemical structure of PVP-I (left) and MADQUAT (right).

Differently from previously published works, our goal is to achieve a high dosing percentage, with 60% of the cathode mass composed of $LiCl + LiI$. This marks the first instance where both salts have been integrated onto the cathode.

The binders are also present, in conjunction with the carbon coating, but they do not constitute the entire cathode matrix. This is illustrated by Zhang et al.[11],

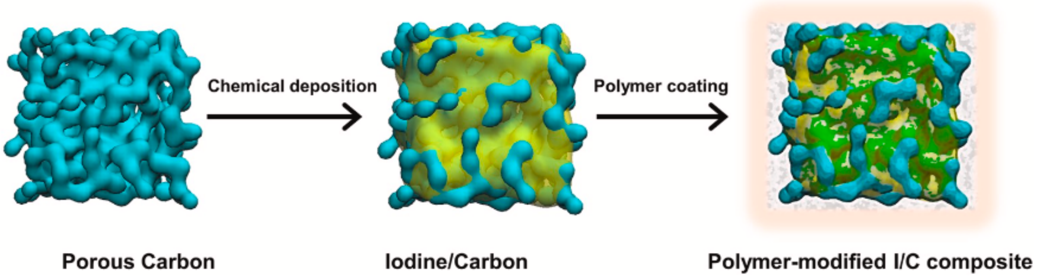

Figure 3.2: Schematic depicting of the fabricating process of the polymer-modified I_2/Porous carbon composites. Adopted and reprinted form [11].

who demonstrate, through TEM and FTIR characterizations, the formation of iodine-based linear inclusion complexes on the surface of composites and good dispersion. The combined effects of the carbon coating and the binder are depicted in Figure 3.2.

We optimized and tested various systems, and all the results are documented in Appendix-C. Following the optimization, a comprehensive comparison was conducted among four different systems. These systems used dosing solutions based on $LiCl$ and LiI in a molar ratio of 1.2, with KB. Subsequently, we varied the binder, choosing from PVP, MADQUAT, a mixture of PVP and MADQUAT (1:1 wt.), or the complete absence of a binder, in this case also the KB was absent. Then the dosing solution was dissolved in EtOH. The solution was dispensed onto the cathode and then subjected to baking at 200°C to remove the solvent.

Throughout all the tests, the conditions remained constant. The electrolyte consisted of $LiTFSI$, $LiNO_3$, $LiBOB$, DOL, DMI, $TEGDME$, and EC. The results were obtained by conducting the rate test described in the methods section.

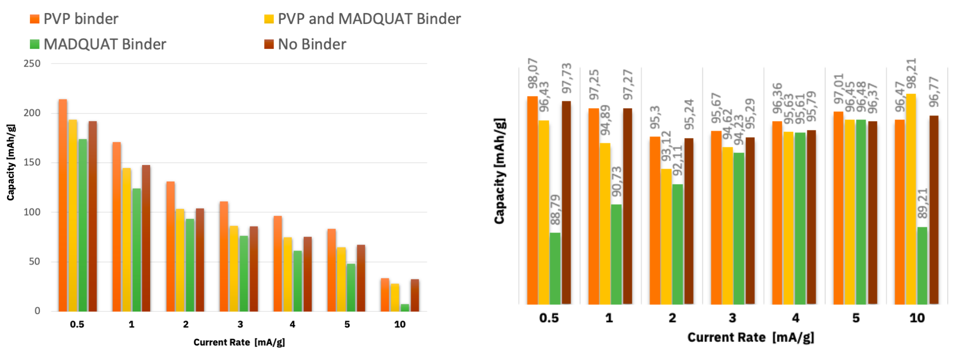

(a) (b)

Figure 3.3: Representations of Capacity (left) and Coulombic efficiency (right)

The obtained results, as plotted in Figure 3.3, do not clearly demonstrate the binder's positive effect on performance. MADQUAT appears to have a consistently adverse effect on performance, degrading capacity at all rates and reducing Coulombic efficiency. It seems that the cumulative effect of the binder hinders the vital role of the carbon coating, occupying the pores without yielding any significant impact.

On the contrary, as previously suggested by several papers, PVP appears to have a positive effect on overall performance. However, it is essential to note that the carbon coating likely plays the most crucial role, as evidenced by the excellent results of the 'No Binder' sample.

Additionally, from the Coulombic efficiency graph, we can gain insight into the shuttling of iodine and chloride compounds. As shown in the graph, PVP slightly improves CE, but the effect is not critical. Analyzing the Coulombic efficiency graph allows us to assess how the choice of the binder reduces shuttling. The trend is quite constant at all rates and shows that the two best systems are with only PVP or without binders.

The only point that significantly deviates from the trend is the CE of the cell where MADQUAT and PVP working together. At high rates, this value is the highest among all the measurements. Binding chloride into the cathode appears to have a significant effect at high rates, but in this case, PVP is essential. The MADQUAT probably occupies a significant portion of the carbon coat pores, hindering the trap effect of the carbon matrix and making the chemical binding of iodine, provided by the PVP, more impactful.

The overall capacity under these conditions is reasonable. The effect can be further interpreted as MADQUAT having a positive impact, maintaining the active material close to the cathode, but it only slightly slows down the dissolution process of chloride compounds. Thus, only at high rate the effect is visible. Indeed, the value associated with only the MADQUAT represents the absolute minimum of CE during all the test. This is because we cannot trap the iodide compound with either PVP or the carbon coating, and the binder likely hampers diffusion due to its steric hindrance.

3.2 Comparison dissolution and integration

The section analyzes the juxtaposition between dissolving $LiCl$ in the electrolyte and physically integrating it into the cathode. Henceforth, the term **dissolution** will refer to $LiCl$ in the electrolyte, while **integration** will pertain to $LiCl$ in the cathode.

We observe how these two different approaches behave and explore the potential reasons for their differences. One of the primary motivations for integrating $LiCl$ into the cathode is to minimize the interaction of the SEI with chloride, mitigate issues related to the low solubility of $LiCl$, and enhance high-rate performance by limiting diffusion time.

3.2.1 Integration effect

In this case, the tests are performed using the same electrolyte and the same ratio of LiI to carbon mass, which is approximately 70

The dosing solution for the cathode that integrates $LiCl$ is composed of $LiCl$ and LiI, along with PVP and KB dissolved in EtOH.

The electrolyte for the two dissolved cells is supplemented with $LiCl$ in the electrolyte. It's worth noting that the mass of $LiCl$ must be in a molar ratio higher than 1.2 with respect to LiI. Specifically, it has a higher molar ratio of $LiCl/LiI$, approximately 1.7, compared to the ratio for the integrated system, which is about 1.25.

The comparison is depicted in Figure 3.4, and the trend clearly shows different behavior.

The performance of the integrated cathodes is nearly as good as the dissolved ones, especially at low rates, demonstrating the viability of this solution. It may inspire a new approach to designing the cathode for the Li/ICl system. The conversion is nearly complete for both the dissolved and integrated systems, with slightly better performance observed for the dissolved system, particularly when the reaction is completed, providing slightly better performance while utilizing a higher mass of active material. A complete conversion had the characteristic that all the iodide completely react not only form $I^+ \rightarrow I^0$ but also the second step is complete $I^0 \rightarrow I^-$.

However, upon examining the area within the red square, it becomes evident that the roles are reversed at high rates. The integrated system appears to be capable of delivering significantly enhanced performance at higher rates. The primary factors influencing this phenomenon are likely the presence of KB and the reduced distance between the two elements responsible for initiating the second electron release.

When comparing the data from the previous section, it appears that the KB effect may not have a substantial impact on high-rate performance. Indeed the 'No Binder' cells of the previous section have no KB but the performance were close to the others, thus probably the higher conductivity has not a major impact on the high rate increased performances. Conversely, when observing the capacity values and the shape of the charge/discharge Galvanostatic curve at elevated rates, it suggests that only the initial step of the reaction is occurring, as described in Equation 1.5. However, in the integrated system, at least a portion of the second step can be harnessed, resulting in a significant capacity increase. This can be attributed to the reduced diffusion time, allowing the second step to consistently occur even at high rates.

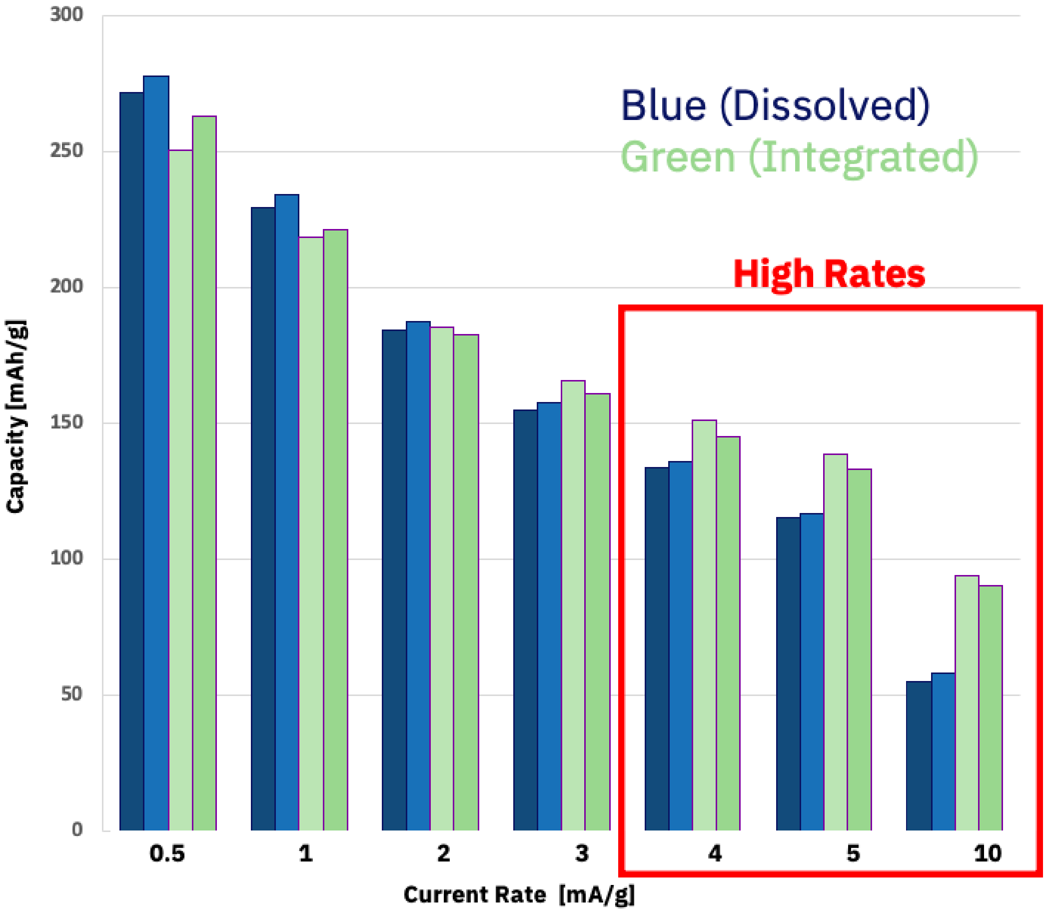

Figure 3.4: Direct comparison between integrated and dissolved systems.

3.2.2 Diffusion-Limited Process

Among our primary goals for the batteries, achieving high-rate capability stands out. As previously discussed, one approach to enhancing the rate capability of a $Li - I - Cl$ battery could be to localize $LiCl$ in proximity to LiI. This strategy minimizes diffusion-related limitations for reactants at high rates.

In a simplified one-dimensional scenario, we can describe the diffusion process of $LiCl$ using Fick's second law of diffusion:

$$\frac{\partial C}{\partial t} = D\frac{\partial^2 C}{\partial x^2} \tag{3.1}$$

Where: - C is the concentration of $LiCl$, - t is time, - D is the diffusion coefficient of $LiCl$, - x is the spatial coordinate along the cathode.

The concentration profile of $LiCl$ will evolve over time according to this equation, influencing the overall availability of reactants for the battery reactions.

By solving this diffusion equation under appropriate boundary conditions (e.g., C remains constant at the interface between the cathode and electrolyte, and imagining the two electrodes are extremely far apart, we can assume that the concentration of $LiCl$ at the anode is constant $[LiCl]_0$), we can determine how the concentration of $LiCl$ changes over time and distance.

The diffusion of $LiCl$ impacts the rate at which it can react with LiI to form ICl, which contributes to the overall battery capacity. At higher rates (currents), this diffusion limitation becomes more pronounced, as the rate of consumption of reactants at the cathode interface increases. This can result in a decrease in battery performance, as the reaction rate becomes limited by the availability of $LiCl$ near the LiI.

In conclusion, localizing $LiCl$ near LiI in the cathode can mitigate diffusion limitations, especially at high rates. This strategy ensures a more efficient utilization of reactants and contributes to improved rate capability for the battery. By optimizing the concentration distribution of $LiCl$ in conjunction with other cathode design considerations, it's possible to enhance the overall performance of the $Li - ICl$ battery system.

4

Optimizing LiCl in Electrolyte

The electrolyte serves as a crucial component in batteries, facilitating the flow of ions between the cathode and anode. Its key properties, such as ion concentration, composition, and conductivity, can be manipulated to optimize battery performances. By adjusting the electrolyte's ion concentration, one can influence the battery's energy density and capacity. In particular for our system the presence of $LiCl$, obtained by Li et al.[12], as mentioned can significantly improve the energy density and capacity. Further, altering the electrolyte's composition can enhance its chemical stability and safety, reducing the risk of thermal runaway events. In the $Li - I$ system the electrolyte can also decrease the solubility of active material, reducing the shuttling issues. Furthermore, optimizing electrolyte conductivity can improve the battery's charge and discharge rates, and as for the cathode optimization the rate capacity is nowadays the main target for the optimization of batteries.

4.1 Design of Experiment

The electrolyte optimization process represents a promising field for the application of Machine Learning, due to the high number of variables and complexity. This section focuses on optimizing an eight-component electrolyte, which includes 3 salts and 4 solvents among those most commonly used for Li-ion batteries, along with $LiCl$. For these kind of high dimensional variables space the optimization would be extremely challenging, and there is also the possibility of not reaching the absolute maximum of performances.

The conventional approach of optimization would involve changing each variable while keeping the others fixed.

This is necessary to gain a clear understanding of the impact of each component on performance (one-factor-at-a-time). However, this method requires extensive work and may not result in the best optimization[15]. Figure 4.1(a-b-c-d) illustrates how a human would optimize the system in a 2D variable space, while (e-f) demonstrates how a machine learning design of experiment should seek the optimum. The set of figures on the right displays the intensity value for each point. In this approach, the human seeks the maximum intensity along a random horizontal value (green line), and then explores the height where the maximum is located. This can lead to a maximum (a-b) or, as in the example, not (c-d). In contrast, the design of experiment can map the space in a more complex manner, as depicted in figure 4.1(f), providing a more comprehensive and accurate description.

In comparison to a conventional optimization process carried out by a human, our goal was to confirm the advantages of this approach. Specifically, we focused our attention on one figures of merit: capacity. We also monitored the cycle life for deeper analysis and confirmation of the actual significance of the capacity data.

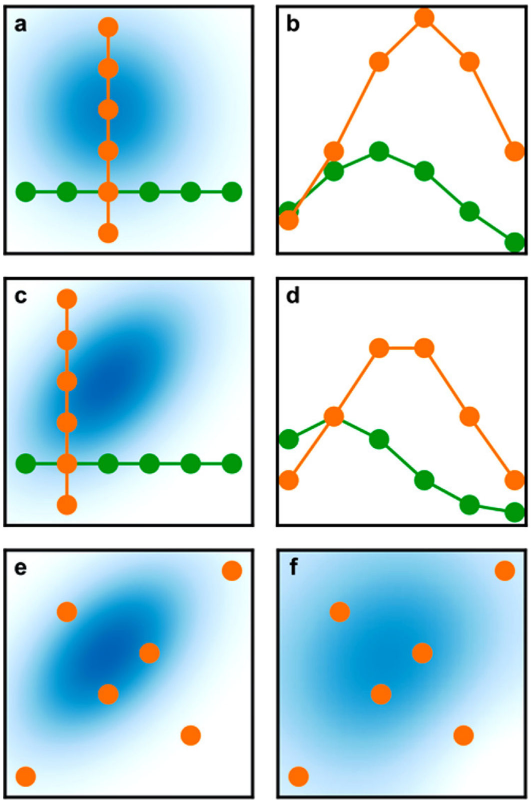

Figure 4.1: Design of experiment, confrontation between a human and a machine approach. Adopted and reprinted from [15].

4.1.1 Salt and solvent concentration ranges

To begin, we have to select data-points well spread and distributed in the variable space. Thus, we have to defined the variable space for optimizing an eight-component electrolyte. Since our system utilizes a completely liquid electrolyte, we excluded compositions that are not entirely soluble.

To determine the boundaries, we conducted a solubility tests for each salt in different mixtures of the four solvents, reported and summarized in Table 4.2. The tests involved adding one salt to a solution until no further dissolution was possible, incrementing by 0.25 M. We determined this point when the salt remained visible after stirring for 12 hours at 450 rpm.

Subsequently, we created an eight-dimensional grid encompassing the possible compositions, with variations spaced at intervals of 100 μl of solvent and 0.1 M of salt.

Table 4.1: Solubility table, of each solvent in different mixtures of solvents(1:1:1:1, 1:1:1:2, 1:1:2:1, 1:2:1:1, 2:1:1:1 by volume of DOL:EC:TEGDME:DMI).

	Solution 1	Solution 2	Solution 3	Solution 4	Solution 5
$LiNO_3$	3.75 M	3.50 M	3.50 M	2.75 M	4.50 M
LiBOB	3 M	2.25 M	2.75 M	2.75 M	2.75 M
LiTFSI	5 M	5 M	5 M	5 M	5 M
LiCl	2.75 M	2.75 M	2.50 M	2.50 M	3.75 M

Table 4.2: Composition of the different solvents mixtures in μl

Solution	**DMI [μl]**	**DOL [μl]**	**EC [μl]**	**G4 [μl]**
Solution 1	250	250	250	250
Solution 2	200	200	200	400
Solution 3	200	200	400	200
Solution 4	200	400	200	200
Solution 5	400	200	200	200

4.1.2 Data Collection

The data acquisition has a key-role in the accelerate discovery process, the low variance of the dataset is crucial for a reliable analysis.

All the data points were collected in our lab, the experimental data contain information about the molar composition of the electrolyte, and capacity and cycle life of the battery, during the test.

The measure performed is a "cycle life test", where the battery performs 10 formation cycles at 0.5 mA/cm^2, and then start the test, cycling at 1 mA/cm^2 until the cell fails or the capacity drops below the 80% of the initial value.

The formation cycles should help the formation of a robust SEI layer and optimize the performances.

The values of capacity used in the process correspond to the initial capacity after the formation cycles. The cycle life corresponds to the number of cycles above the 80% of the initial capacity, the formation cycles are not counted.

Table 4.3: Experimental 28 points, used for training and testing the ML

LiTFSI	LiBOB	LiCl	LiNO3	DOL	EC	G4	DMI	CAP [mAh/g]	CYC
2.9	17.4	7.4	0.7	20.3	10.9	6.8	33.7	6.1	24
1.9	4.4	7.6	5.2	48.5	10.8	3.1	18.4	146.6	20
10.6	5.6	6.7	4.9	50.6	7.8	2.8	11.0	70.4	55
7.1	1.3	14.2	7.7	18.8	19.6	5.8	25.5	72	20
3.0	14.9	8.9	2.4	20.6	11.2	9.9	29.1	11.5	190
15.5	1.7	1.7	0.7	35.0	34.7	5.4	5.3	124.7	30
1.2	9.8	13.6	5.0	34.7	9.3	3.0	23.3	56.3	16
10.5	3.1	1.4	13.4	50.6	9.0	5.8	6.2	128.1	81
5.0	2.9	10.8	4.3	20.3	33.0	10.0	13.7	81.4	73
2.7	17.5	0.7	9.8	18.7	9.8	3.6	37.1	0.7	5
1.9	12.5	0.6	7.2	13.7	30.2	7.2	26.7	4.3	6
8.7	0.6	7.2	3.8	8.2	56.7	3.2	11.6	136.0	45
1.7	11.1	0.4	6.3	12.2	38.7	5.9	23.7	24.6	582
8.9	5.5	15.5	1.3	27.8	9.9	3.1	32.0	107.1	6
0.7	6.7	9.6	12.6	9.5	19.3	3.4	38.2	11.2	136
9.5	17.6	1.3	2.1	9.8	30.2	9.8	19.6	3.4	31
9.0	0.7	10.1	6.9	9.5	41.3	9.9	12.7	0.6	17
1.9	5.1	10.1	7.5	26.5	28.3	3.0	17.7	114.6	81
13.4	2.0	10.7	4.9	27.9	9.9	6.2	24.9	113.1	14
7.5	6.9	13.5	2.5	17.6	37.5	8.8	5.6	103.5	32
10.5	1.3	6.8	3.1	54.1	9.4	3.0	11.9	133.1	20
3.0	7.0	19.1	2.4	20.9	22.3	18.1	7.2	60.6	82
1.1	7.8	16.0	14.1	11.9	12.6	28.4	8.0	14.9	735
11.7	2.5	3.3	16.1	0	12.1	15.7	38.5	9.2	340
2.6	15.8	6.8	0.8	28.1	18.6	3.2	24.1	1.9	82
22.2	1.9	2.6	0.9	46.0	0	19.2	7.2	102.8	4
2.2	5.1	7.3	5.6	56.2	47.7	0	0	153.8	10
6.6	1.7	18.3	9.9	68.0	0	0	29.3	55.8	5

Between all the possible composition we select a well distributed ensemble of electrolytes, and test those. We collect more than 60 datapoints and the complete dataset is reported in the Appendix A, then we short list 28 points between those, minimizig the variability due to experimental uncertainty and errors. The selected points are reported in table 4.3.

This dataset map the variable space in a unbiased and distributed manner, to confirm this, we report also the box plot, where for each component is analysed the molar percentage distribution, figure 4.2.

The 28 points are then summarized in the following table, using the pandas function df.describe() in python, to evaluate the actual distribution of the electrolyte compositions.

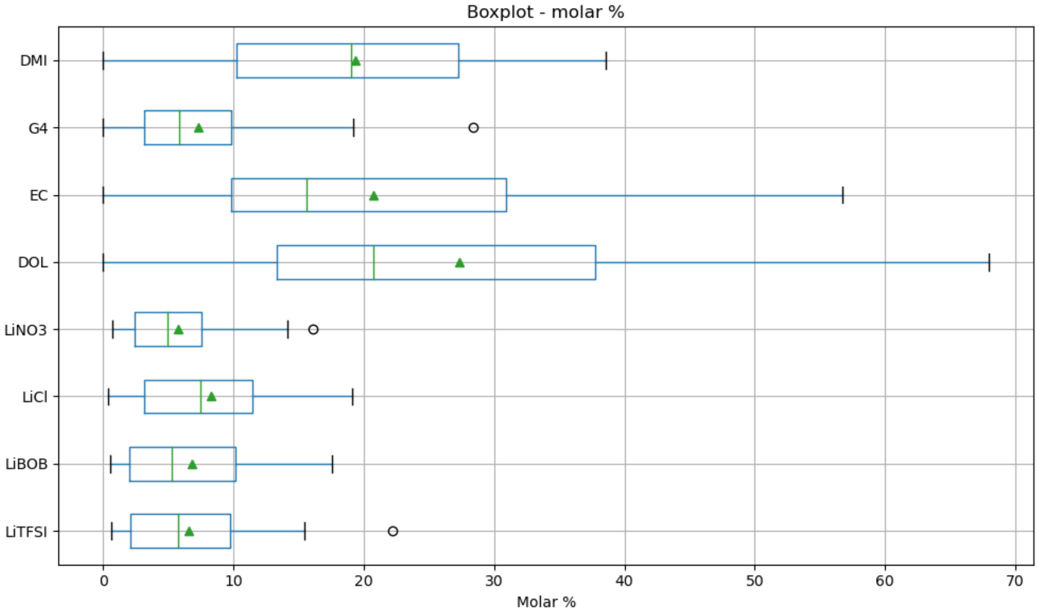

Figure 4.2: Box representation of components distribution. The box in the middle of the plot represents the middle 50% of the data, often referred to as the interquartile range (IQR).The lines, or whiskers, extend from the box to the smallest and largest values within 1.5 times the IQR. The triangle represents the average value, the circles represent the outliers point.

Table 4.4: Statistical description of independent variables

	LiTFSI	LiBOB	LiCl	LiNO3	DOL	EC	G4	DMI
count	28.000	28.000	28.000	28.000	28.000	28.000	28.000	28.000
mean	6.553	6.799	8.293	5.795	27.362	20.741	7.301	19.367
std	5.249	5.606	5.532	4.335	17.571	14.706	6.369	11.218
min	0.664	0.591	0.423	0.715	0.000	0.000	0.000	0.000
25%	2.119	1.979	3.138	2.418	13.313	9.869	3.143	10.267
50%	5.792	5.308	7.476	4.970	20.754	15.605	5.809	19.021
75%	9.783	10.157	11.468	7.548	37.743	30.900	9.829	27.268
max	22.233	17.582	19.078	16.064	67.980	56.685	28.426	38.532

Further, we analyse the correlation between the variables and the two figures of merit, we exploit the Pearson coefficient and the heatmap of the correlation. The Pearson coefficient evaluate the correlation between two variables, it express between -1 and 1 the correlation, as shown in eq.4.1, 4.2.

$$cov(X,Y) = \sum \frac{(X- < X >)(Y- < Y >)}{N} \tag{4.1}$$

$$corr(X,Y) = \frac{cov(X,Y)}{\sigma_x \sigma_y} \tag{4.2}$$

This analysis allows us to ascertain macroscopic trends in the performance metrics associated with each individual electrolyte component. The Pearson coefficient calculation is carried out sequentially for each variable, and the outcomes are visually depicted in the two heatmaps shown in Figure 4.3. These heatmaps offer a preliminary analysis of the variables with the performance metrics and guide us to understand relationship. As expected, there exists an inverse correlation between capacity and cycle life. However, this correlation doesn't entirely preclude the potential for discovering an optimal trade-off between the two performance indicators.

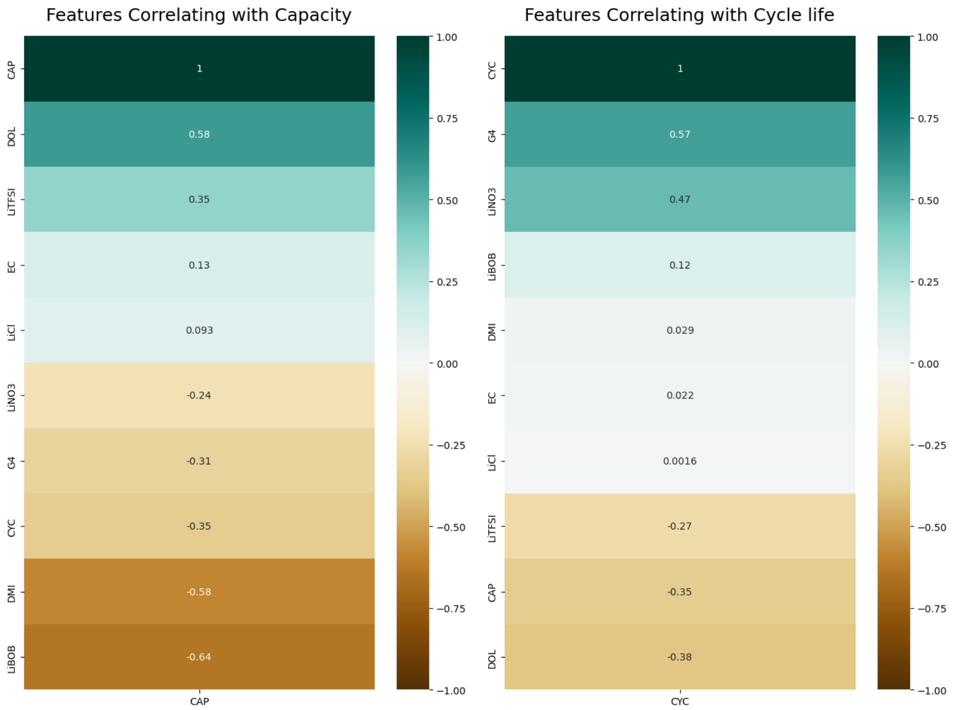

(a) (b)

Figure 4.3: Heatmaps for correlation between the 8 independent variables on the left the variable-capacity PC and on the right the variable-cycling life PC.

Conversely, $LiBOB$ exhibits a significant inverse correlation with cell capacity within the tested range. This relationship is particularly evident in Figure 4.4, which showcases the Pearson coefficient. Notably, an excessive presence of $LiBOB$ appears to negatively impact cell performance. Specifically, when $LiBOB$ concentrations exceed 7%, the correlation becomes even more pronounced, with a Pearson coefficient of -0.763. However, for concentrations below 7%, establishing a distinct trend isn't straightforward, leading to a low Pearson coefficient of 0.044.

This interpretation is admittedly simplified, as it centers on a single variable and endeavors to establish a linear correlation for a metric that likely possesses at least one maximum point. Nevertheless, it offers intriguing insights into the characteristics of salts and their effects on cell performance.

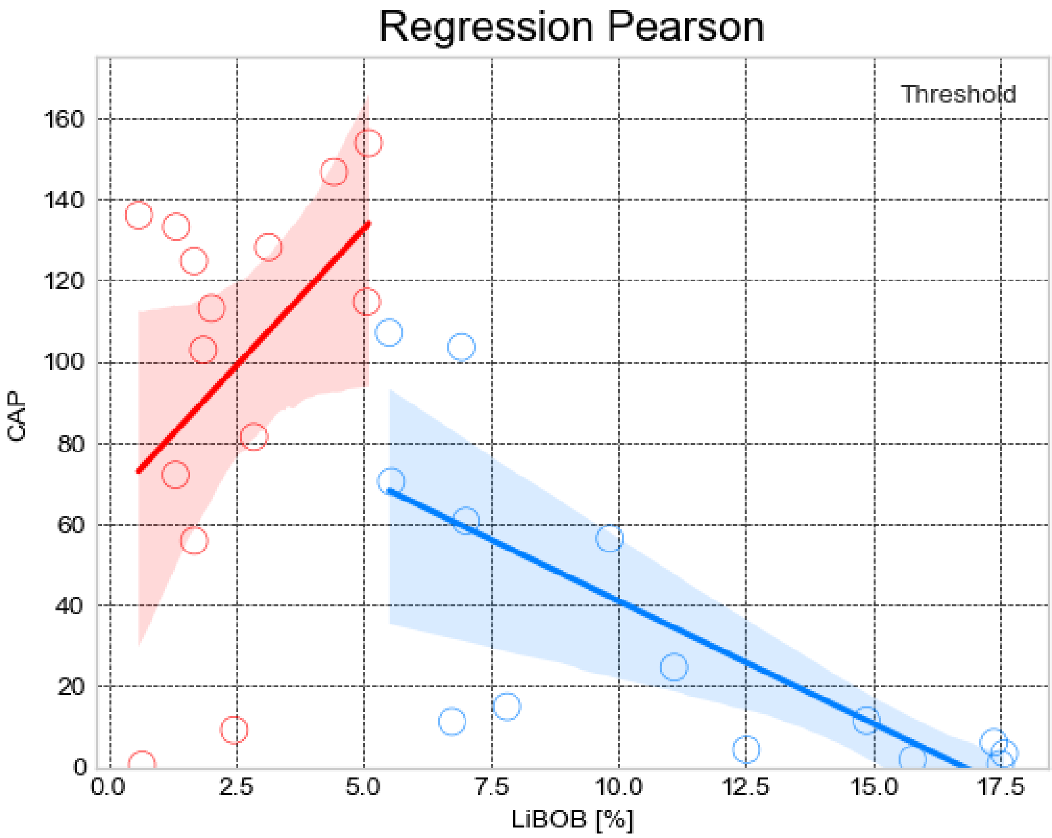

Figure 4.4: Pearson coefficient of $LiBOB$ concentration in molar percentage and capacity.

4.1.3 Machine Learning

For the Machine Learning process, we evaluated several regression supervised learning algorithms, reported in Appendix-B, and shortlisted three: Linear Regression, Random Forest Regression, and Support Vector Regression. These models were used to fit the data and explore the relationships between electrolyte compositions and performance metrics.

For the best models, in particular the Random Forest Regressor, we perform a optimization of the hyperparameter, using Bayes Search CV and Grid Search CV, both technique implemented in Python using scikit-learn.

One of the primary hyperparameters to consider is the number of trees in the forest, denoted as "**n_estimators**". This parameter controls the number of decision trees that are trained and combined in the ensemble. Bayesian optimization can help find the optimal value for n_estimators by evaluating its impact on both training and validation performance.

Another crucial hyperparameter is the depth of each decision tree, known as "**max_depth**". This hyperparameter governs the complexity of individual trees and plays a significant role in preventing overfitting.

The "**min_samples_split**" and "**min_samples_leaf**" hyperparameters determine the minimum number of samples required to split an internal node and the minimum number of samples required to be a leaf node, respectively. Tuning these hyperparameters can contribute to improving the Random Forest's ability to generalize to new data.

Additionally, the "**max_features**" hyperparameter controls the number of features considered for the best split at each node. Bayesian optimization can help pinpoint the optimal value of max_features to enhance model diversity and robustness. By tuning hyperparameters like n_estimators, max_depth, min_samples_split, min_samples_leaf, and max_features, you can fine-tune your Random Forest model to achieve the best possible performance for your specific machine learning task.

In particular, we perform 5-fold cross validation where the data are divided in 5-fold, four are used for training the model and the remaining one is used as validation. During the 5-fold cross validation the algorithm is tested and the hyperparameter are modify until a maximum in the accuracy is reached.

The best tuned hyperparameter are then used for the fitting of the datapoints, in the Random Forest the gain in the accuracy is remarkable, Figure 4.9.

The performances obtained are reported in Figure 4.5, 4.6, 4.7, 4.8, combining the fitting and the cross validation results, is possible to observe that tuned random forest obtain the best trade off between under and over fitting.

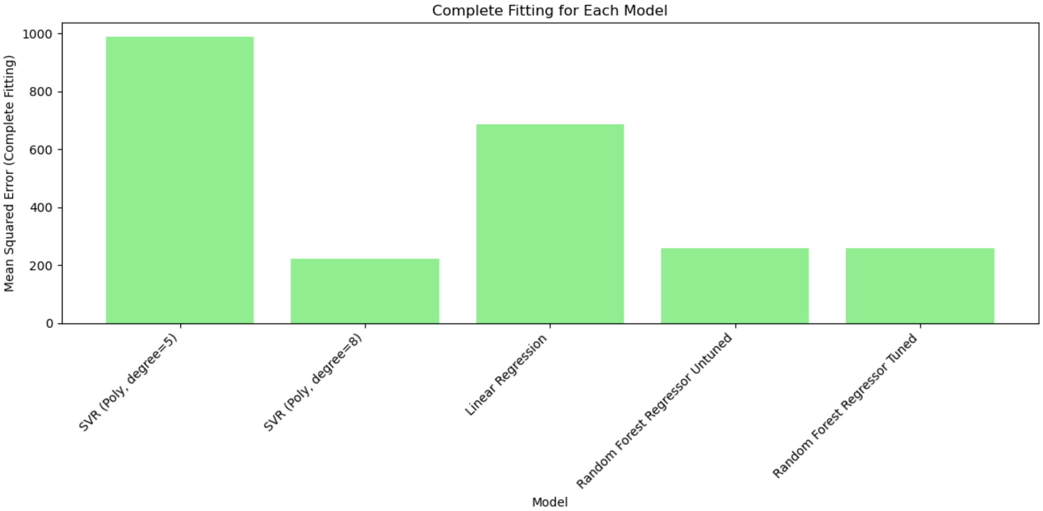

Figure 4.5: Fitting MSE performances of the shortlisted methods.

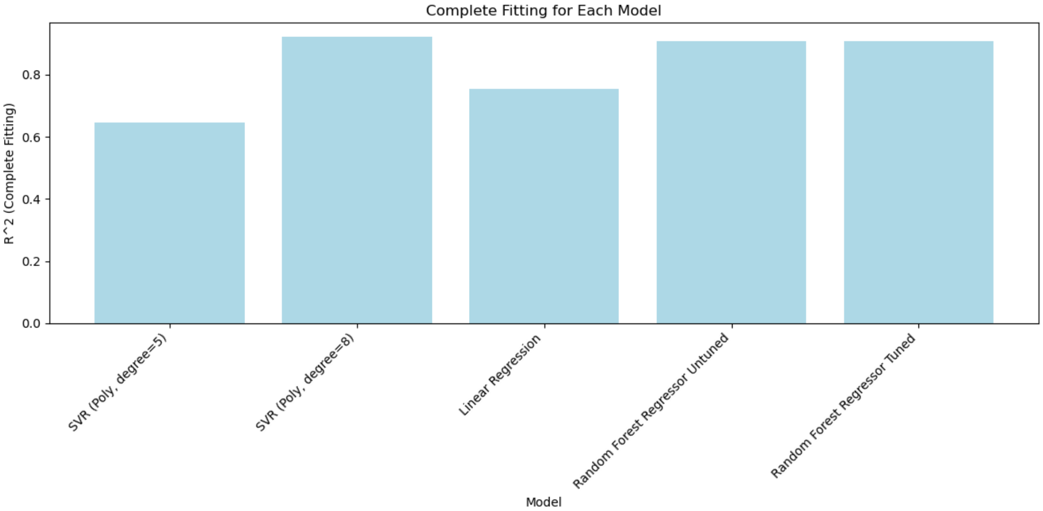

Figure 4.6: Fitting R^2 performance of the shortlisted methods.

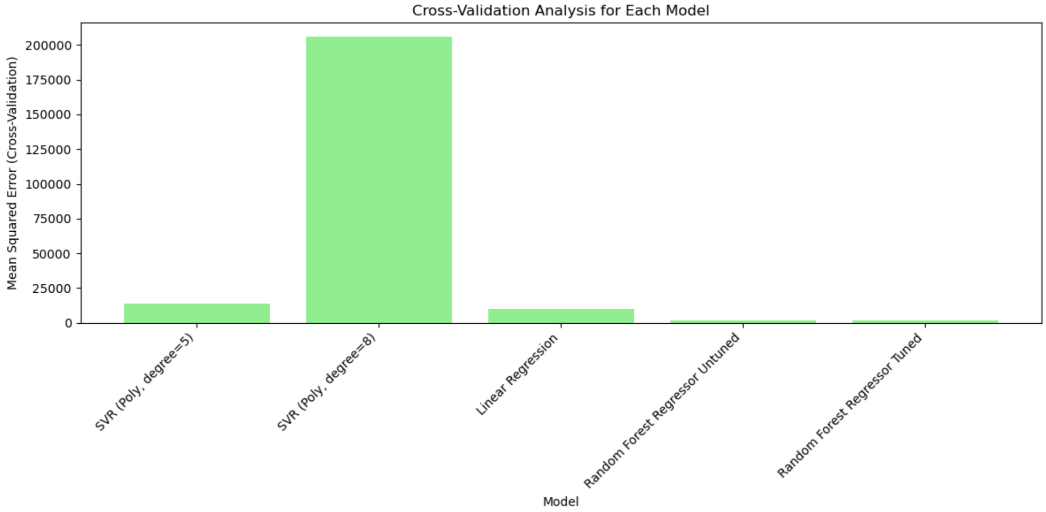

Figure 4.7: Cross validation MSE performances of the shortlisted methods.

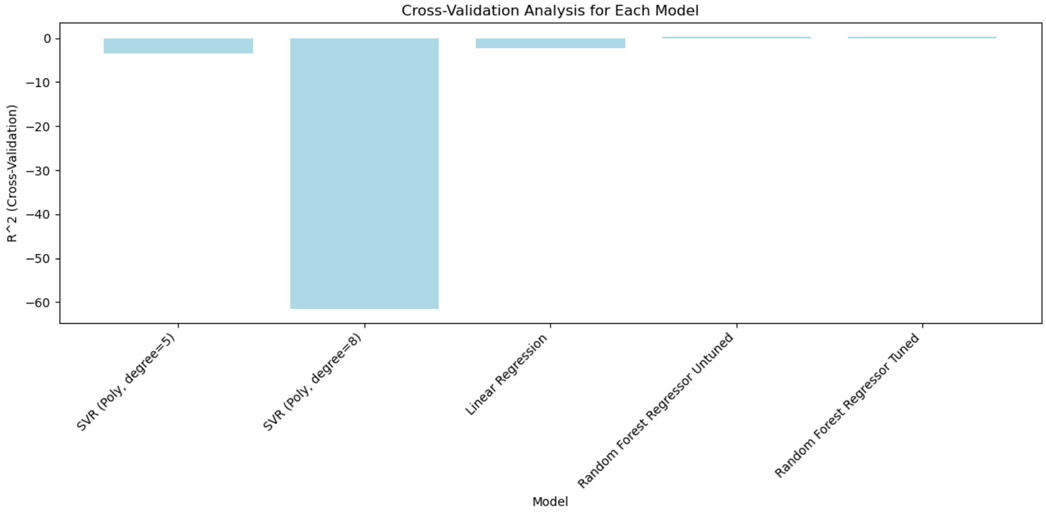

Figure 4.8: Cross validation R^2 performances of the shortlisted methods.

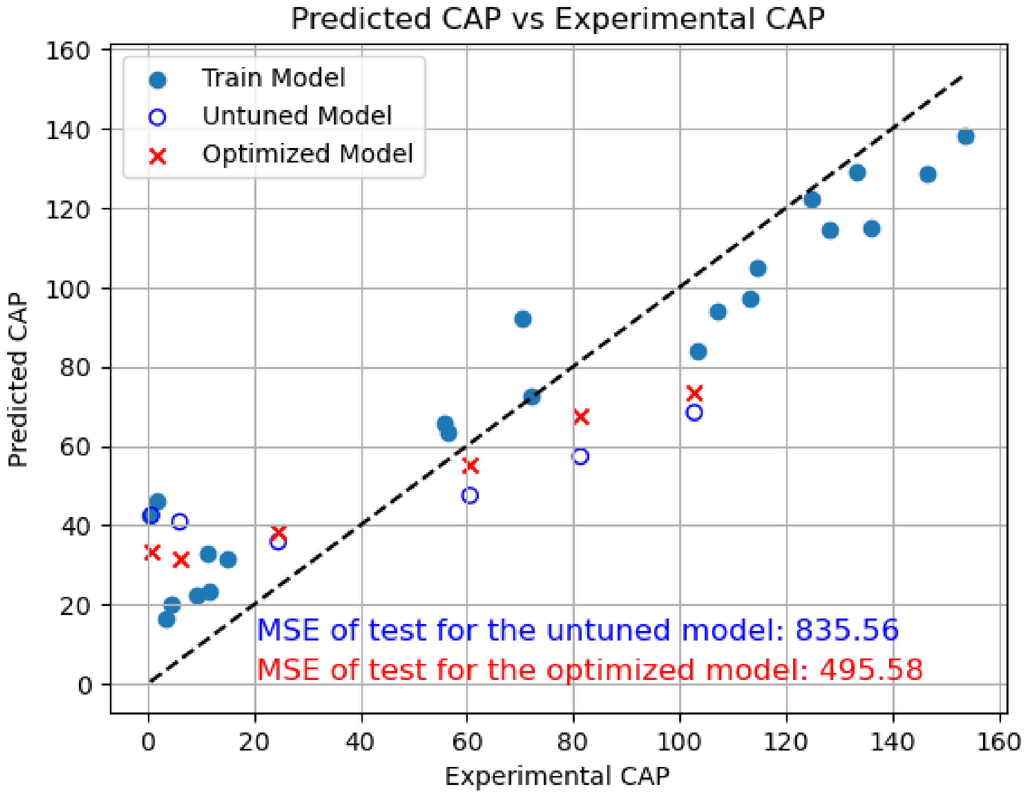

Figure 4.9: Performances of the tuned and untuned models.

Individual correlations

Now we analyse the influence and correlation, of every possible combination of input variables with the capacity exploiting the random forest regression, reported in Table 4.5. The accuracy shows that some isolated variables are able to fit precisely the behavior of a system that includes many more variables. This highlight the collaboration of certain elements that have a coordinated impact on the performances.

For the top two combinations of two salts, we create a three-dimensional visualization illustrating how the fitted capacity varies with different combinations of the variables. A high level of accuracy implies the model's ability to effectively fit the variables and establish a strong correlation with the performance metric.

Table 4.5: Best Combinations of variables for capacity, and corresponding average R^2, 5 fold cross validation.

LiTFSI	LiBOB	LiCl	LiNO3	DOL	EC	G4	DMI	Average R^2
0	1	0	0	0	0	0	0	0.0672147
0	0	0	0	0	0	1	0	-0.0839108
0	1	0	1	0	0	0	0	0.400458
0	1	0	0	0	0	1	0	0.348557
0	1	0	1	1	0	0	0	0.444567
0	1	0	1	0	0	1	0	0.437912
0	1	0	1	1	0	1	0	0.476795
0	1	1	1	0	0	1	0	0.44902
0	1	1	1	1	0	1	0	0.483798
0	1	0	1	1	1	1	0	0.460001
0	1	1	1	1	1	1	0	0.488435
1	1	1	1	1	0	1	0	0.44927
1	1	1	1	1	1	1	0	0.44563
0	1	1	1	1	1	1	1	0.417142
1	1	1	1	1	1	1	1	0.371607

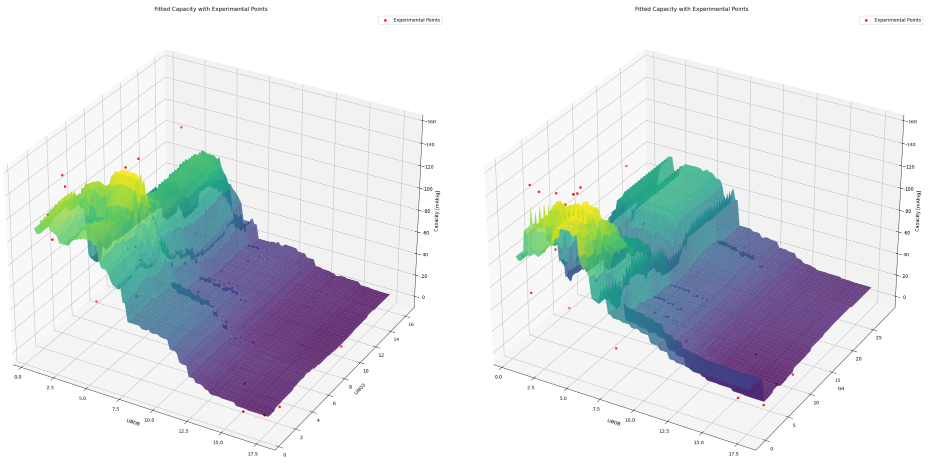

(a)

(b)

Figure 4.10: Two variable correlation, with the capacity. Red dots represent the experimental points.

With just 28 data points, machine learning is able to achieve a high level of accuracy for fitting and cross-validation. This demonstrates the viability of our solution. The careful selection of hyperparameters and the choice of the most suitable algorithm are clearly critical steps in designing an effective model.

The ability to create a model that can produce such results is promising for future research steps, especially when working with larger datasets. Artificial intelligence will undoubtedly play a significant role in understanding the intricate relationships between components and performance, where the human eye often struggles to distinguish between different contributions. These results set us on a promising path for further discoveries and insights in this field.

5

Conclusion

The focus of my research has been on optimizing both the electrolyte and cathode components of a promising and high-performing battery system. While there are still multiple challenges to address, this work demonstrates the potential of using artificial intelligence (AI) to support discoveries in this field.

Our AI model has achieved remarkable results in fitting and cross-validate the input, even with a very limited dataset. This suggests that further exploration in this area could significantly contribute to optimizing not only this specific system but also the high-entropy materials in general. The choice of an appropriate model and optimization strategy is crucial, as it relies on collecting well spread data points with low variability and high reliability.

Exploring new strategies and specific approaches for data analysis in this highly complex and hard to explore domains is also of utmost importance.

On the cathode optimization side, we've gained valuable insights into the potential of this system. Diffusion and surface phenomena have a direct and noticeable impact on cell performances. The ability to integrate all active materials onto the cathode appears to enhance performance at high rates while maintaining good performance at lower rates. This opens up new possibilities for understanding the underlying causes and intricate relationships, ultimately offering a path to increasing capacity and performance.

The research is still an ongoing process and this work is a intermediate step that can help the future process of optimization and design of next-gen batteries for a greener. The Lithium-Iodine battery continue to show outstanding performances and they are increasing their stability and cycling life, they are good candidates for future high rate application as required by the electric vehicle market.

Bibliography

[1] Brudermüller Martin et al. „A Vision for a Sustainable Battery Value Chain in 2030“. In: *Global battery alliance* (2019), p. 51.

[2] Mustafa Ergin Şahin, Frede Blaabjerg, and Ariya Sangwongwanich. „A comprehensive review on supercapacitor applications and developments“. In: *Energies* 15.3 (2022), p. 674.

[3] John B Goodenough. „How we made the Li-ion rechargeable battery“. In: *Nature Electronics* 1.3 (2018), pp. 204–204.

[4] Naoki Nitta et al. „Li-ion battery materials: present and future“. In: *Materials today* 18.5 (2015), pp. 252–264.

[5] Huiming Wang et al. „Recent advances in conversion-type electrode materials for post lithium-ion batteries“. In: *ACS Materials Letters* 3.7 (2021), pp. 956–977.

[6] Seung-Ho Yu et al. „Understanding conversion-type electrodes for lithium rechargeable batteries“. In: *Accounts of chemical research* 51.2 (2018), pp. 273–281.

[7] Arumugam Manthiram, Yongzhu Fu, and Yu-Sheng Su. „Challenges and prospects of lithium–sulfur batteries“. In: *Accounts of chemical research* 46.5 (2013), pp. 1125–1134.

[8] Lei Zhang and Xiong Wen Lou. „Hierarchical MoS2 shells supported on carbon spheres for highly reversible lithium storage“. In: *Chemistry–A European Journal* 20.18 (2014), pp. 5219–5223.

[9] Feipeng Yang et al. „MoS2 for beyond lithium-ion batteries“. In: *APL Materials* 9.5 (2021).

[10] Qing Zhao et al. „Rechargeable lithium-iodine batteries with iodine/nanoporous carbon cathode“. In: *Nano letters* 15.9 (2015), pp. 5982–5987.

[11] Qian Zhang et al. „Inclusion complexation enhanced cycling performance of iodine/carbon composites for lithium–iodine battery“. In: *Journal of Power Sources* 463 (2020), p. 228212.

[12] Xinliang Li et al. „Two-Electron Redox Chemistry Enabled High-Performance Iodide-Ion Conversion Battery“. In: *Angewandte Chemie* 134.9 (2022), e202113576.

[13] Maxwell J Giammona et al. „Oxygen Assisted Lithium-Iodine Batteries: Towards Practical Iodine Cathodes and Viable Lithium Metal Protection Strategies“. In: *Advanced Materials Interfaces* (2023), p. 2300058.

[14] S Siggia. „The chemistry of polyvinylpyrrolidone-iodine“. In: *Journal of the American Pharmaceutical Association (Scientific ed.)* 46.3 (1957), pp. 201–204.

[15] Bing Cao et al. „How to optimize materials and devices via design of experiments and machine learning: Demonstration using organic photovoltaics“. In: *ACS nano* 12.8 (2018), pp. 7434–7444.

6

APPENDIX-A

6.1 Training tests

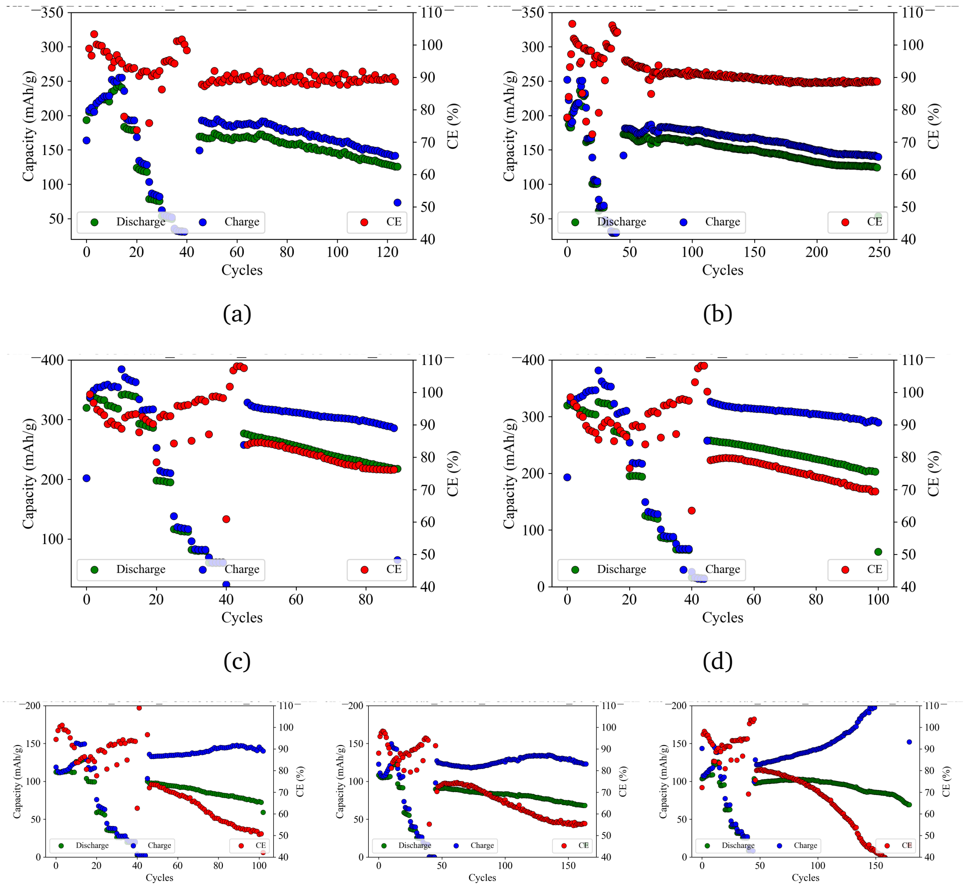

(a)

(b)

(c)

(d)

(e)

(f)

(g)

Figure 6.1: Results of the GCPL for the electrolytes design by the AI trained until January. (a-b-c-d) Experiment for 30% dosing. (e-f-g) Experiment at 50 %.

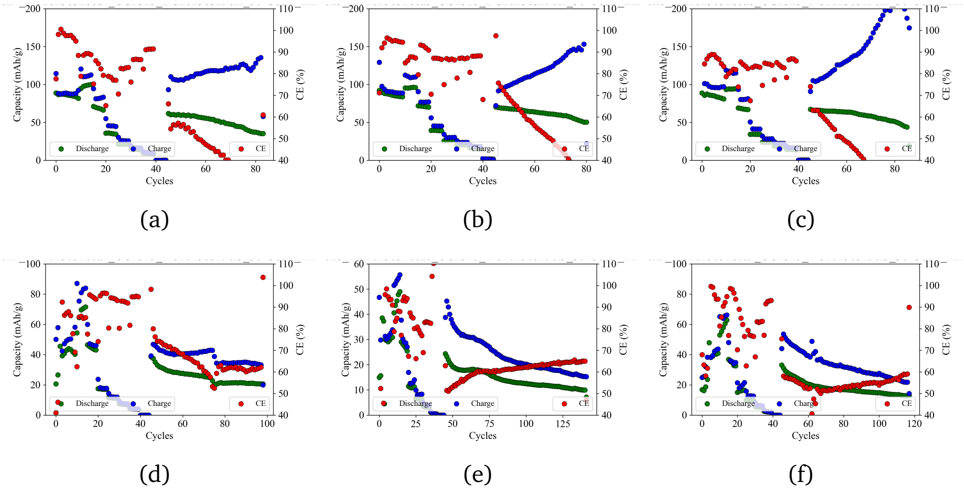

(a) (b) (c)

(d) (e) (f)

Figure 6.2: Results of the GCPL for the electrolytes design by the AI trained until January. (a-b-c) Experiment for 60% dosing. (d-e-f) Experiment at 70 %.

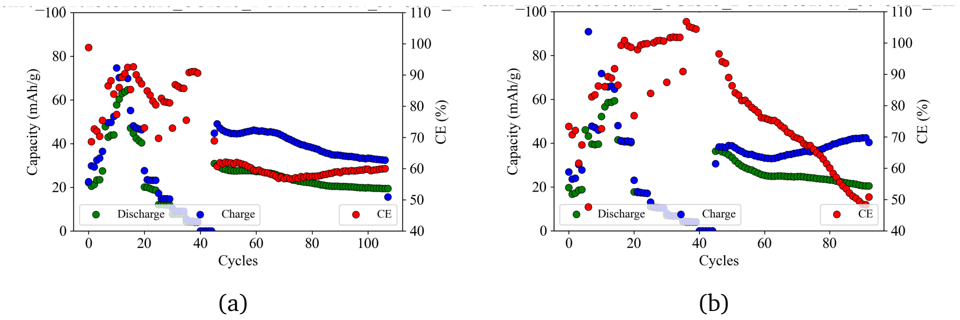

(a) (b)

Figure 6.3: Results of the GCPL for the electrolytes design by the AI trained until March.(a-b) Experiment for 70 % dosing.

The cells' Galvanostatic Cycling with Potential Limitation (GCPL) results are presented in the following figures. Each figure shows the cell's capacity plotted against the cycle number. The blue line represents the capacity during charging, the green line represents the capacity during discharging, and the red line represents the Coulombic Efficiency, which is the ratio of charge to discharge.

It was observed that the predictions were not consistent with the actual results as the dosing increased. In fact, the observed trend was opposite to the predicted trend. This inconsistency can be attributed to the limited number of input elements in the training dataset.

This confirmation analysis also served as a tutorial, allowing me to work closely with cell production and enhance my assembly skills.

6.2 Lithium chloride in electrolyte

The cells were produced to operate a two-electron mechanism, so $LiCl$ has to be included in the chemical reaction. The first approach was to include $LiCl$ in the electrolyte, as this solution had already been tested and it avoids making the dosing process even more complex. The optimized electrolyte composition consisted of the four salts ($LiCl$, $LiNO_3$, $LiTFSI$, $LiBOB$) and three solvents. The main objective of this section was to collect a critical dataset for the training of the AI.

We tested many different solvents, salts, and compositions. The first set of experiments used two alternative solvents (E/F) to substitute solvent A while keeping the salt composition exactly the same. These two new electrolytes were tested, and the results are reported in figure 6.4. It is clear that solvent E is not working, and solvent F is not an optimal solution.

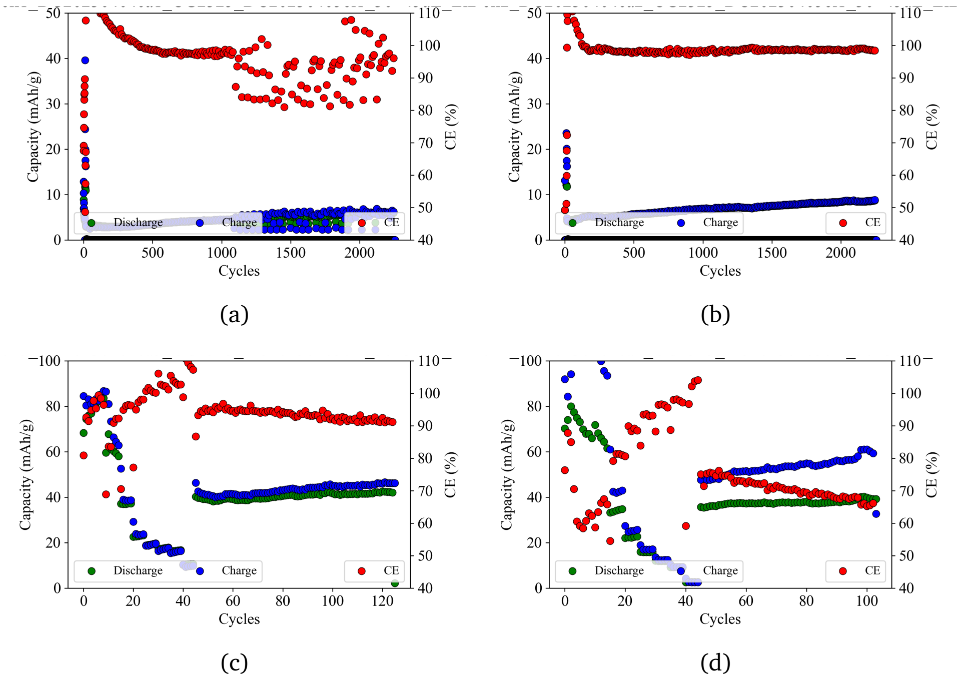

(a)

(b)

(c)

(d)

Figure 6.4: Results trying to substitute the solvent A. Experiment for 55% dosing.(a-b) Cells using solvent E, (c-d) cells using solvent F.

Meanwhile, we also tested solvent D, which required a change in the separator compared to our previous results. We switched from the celgard (CG2325) separator to a quartz microfiber (QMA) separator. This difference should be noted as it contributes to a more accurate description of the systems. The results obtained with the new separator and solvent are reported in Figure 6.5, and they indicate a significant increase in capacity, especially at high rates.

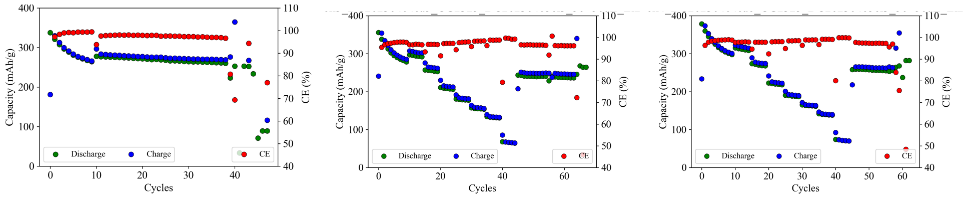

(a) (b) (c)

Figure 6.5: Capacity during the standard GCPL for three cells using solvent D. Experiment for 35% dosing. (a) Cycling life without rate test, (b-c) Standard test.

Afterward, we decided to conduct a comprehensive comparison of the effects of the four solvents (A/B/C/D) by varying the volume ratio of the components. In order to assess the distinct impacts of the solvents, we created five different electrolytes using five different mixtures of the four solvents while keeping the salt constant. All the results were averaged over at least two cells, and the specific capacity was normalized to the mass of iodine, as depicted in figure 6.8. Upon observing the graph, it is important to note that the concentration of solvent D was higher in the K3 formulation. This composition exhibited the highest capacity at high rates, which is crucial for meeting the requirements of the next generation.

Then, we decided to evaluate the optimal volume by conducting tests using the QMA separator. The results are depicted in figure 6.7. By examining the Nyquist plots of the four cells, as shown in figure 6.6, we can analyze the impact of the electrolyte on the behavior of the cells. Typically, the cells are represented as a series connection between a resistance and a parallel combination of resistance and capacitor.

It is evident that Cell 1, with a low electrolyte volume, exhibits a high series resistance of approximately 150 Ω. On the other hand, Cell 2 shows satisfactory results, albeit slightly worse than those of Cells 3 and 4, particularly in terms of high frequency resistance. The Nyquist plot for Cell 3 and Cell 4 appears quite similar, with a slight degradation observed for the 110 μl volume. Based on these findings, it can be concluded that the optimal electrolyte volume is around 100 μl. However, it is worth noting that this may pose a concern due to the slightly higher weight of the electrolyte in comparison to the target values.

Additionally, the electrolyte volume is an important parameter for the AI, and it needs to be considered in the design of an AI system capable of predicting the behavior of a full cell. For our electrolyte optimization, this parameter has been fixed, and henceforth, the electrolyte volume is set at 100 μl.

From the capacity and shuttling results, we can also observe some detrimental effects of the solid/liquid ratio. This could be correlated with the amount of LiCl, which has a negative impact, or with the high quantity of liquid that increases the solubility of iodine species.

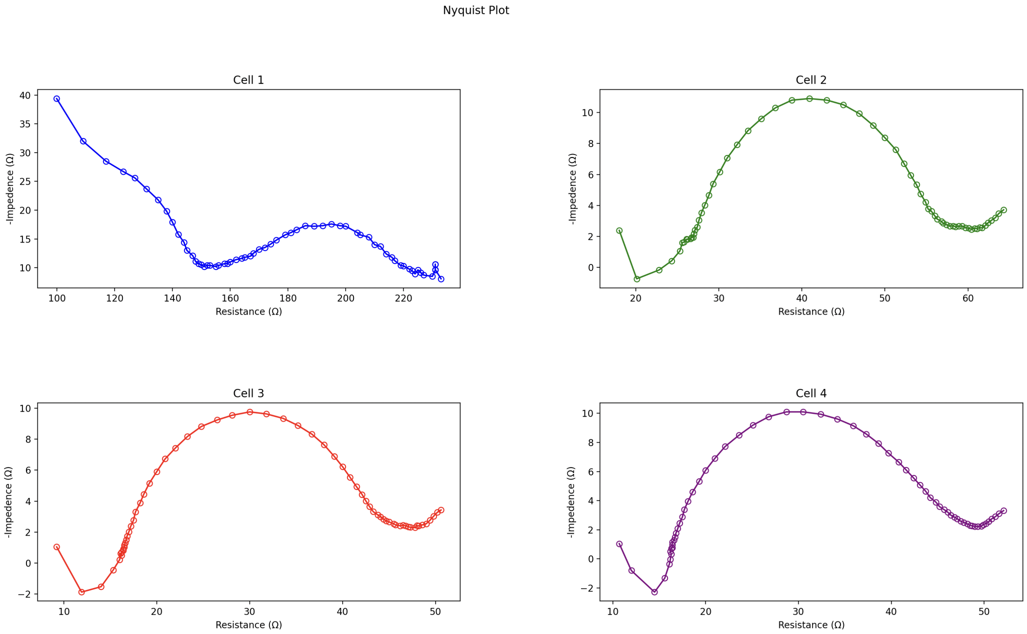

Figure 6.6: Nyquist plot of the electrolyte volumes comparison. (cell 1) 40 μl, (2) 60 μl, (3) 90 μl, (4) 110 μl

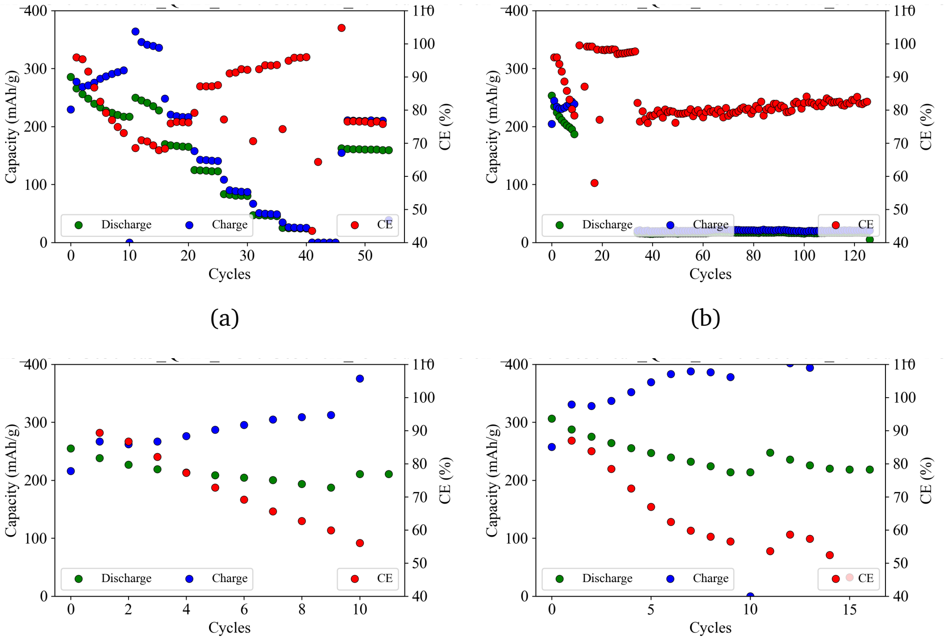

(a)

(b)

(c)

(d)

Figure 6.7: Capacity during the standard GCPL for 4 different volumes of electrolyte. Experiment for 50% dosing. (a) 40 μl, (b) 60 μl, (c) 90 μl, (d) 110 μl

The previous results were obtained for low dosing, so we decided to try increasing the dosing to collect data for high dosing as well. $LiCl$ needs to be added to the electrolyte to facilitate the second electron reaction, as Cl^- can stabilize I^+. Therefore, it is important to maintain a constant molar ratio between the two. Increasing the concentration of $LiCl$ in the electrolyte is not a trivial task due to its low solubility in the solvents used. If we want to increase the concentration of $LiCl$, we also need to increase the volume of solvent A to ensure complete dissolution. From the previous results, it appeared that the electrolyte with a high volume of solvent A (K5) performed less effectively. The results indicate that increasing the dosing leads to shuttling and lower coulombic efficiency, causing the cells to stop working almost immediately. On the other hand, the resistance appears to be relatively low and not limiting.

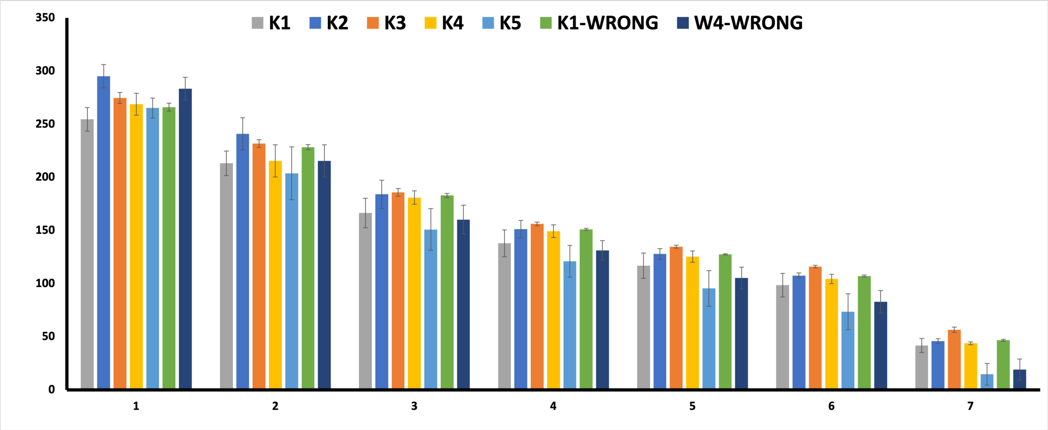

Figure 6.8: Comparison between capacity $[mAh/g]$ of 5 different electrolytes composition at different charge/discharge rates. In Particular $0.5 - 1 - 2 - 3 - 4 - 5 - 10\ mA/cm^2$. Experiment for 40% dosing. There are 2 additional formulation used as reference.

6.3 Data collection

Complete dataset for DoE. COMPOSITION TABLE

NAME_1	NAME_2	LiTFSI	LiBOB	LiCl	LiNO3	DOL	EC	TEGDME	DMI
DC20230519cell1	DC20230519cell2	2.9	17.4	7.4	0.7	20.3	10.9	6.8	33.7
DC20230621cell1	DC20230621cell2	2.9	17.2	7.2	0.7	20.0	10.5	6.8	34.7
DC20230519cell3	DC20230519cell4	1.9	4.4	7.6	5.2	48.5	10.8	3.1	18.4
DC20230621cell3	DC20230621cell4	2.0	4.6	8.4	5.4	47.5	9.8	3.1	19.1
DC20230519cell5	DC20230519cell6	10.6	5.6	6.7	4.9	50.6	7.8	2.8	11.0
DC20230621cell5	DC20230621cell6	10.9	5.8	7.0	5.1	48.5	8.4	2.7	11.4
DC20230519cell7		7.1	1.3	14.2	7.7	18.8	19.6	5.8	25.5
DC20230621cell7	DC20230621cell8	7.1	1.3	14.6	8.0	19.0	19.0	6.1	24.8
DC20230519cell9	DC20230519cell10	3.0	14.9	8.9	2.4	20.6	11.2	9.9	29.1
DC20230621cell9	DC20230621cell10	2.4	14.8	9.0	2.3	21.2	10.7	11.2	28.3
DC20230519cell11	DC20230519cell12	15.5	1.7	1.7	0.7	35.0	34.7	5.4	5.3
DC20230621cell11	DC20230621cell12	15.8	1.1	1.9	0.6	33.5	38.7	2.7	5.7
DC20230523cell1	DC20230523cell2	1.2	9.8	13.6	5.0	34.7	9.3	3.0	23.3
DC20230621cell13	DC20230621cell14	1.2	9.8	13.6	5.0	35.3	8.9	3.3	22.9
DC20230523cell3	DC20230523cell4	10.5	3.1	1.4	13.4	50.6	9.0	5.8	6.2
DC20230621cell15	DC20230621cell16	9.9	1.9	1.4	13.4	53.2	9.2	5.6	5.4
DC20230523cell5	DC20230523cell6	5.0	2.9	10.8	4.3	20.3	33.0	10.0	13.7
DC20230621cell17	DC20230621cell18	5.0	2.8	10.8	4.1	20.0	33.3	10.6	13.4
DC20230523cell7		8.8	14.9	2.0	4.9	18.7	9.8	3.1	37.9
DC20230621cell19	DC20230621cell20	2.7	17.5	0.7	9.8	18.7	9.8	3.6	37.1
DC20230523cell11	DC20230523cell12	2.5	16.3	0.7	9.4	18.4	37.7	9.2	5.7
DC20230621cell21	DC20230621cell22	1.9	12.5	0.6	7.2	13.7	30.1	7.2	26.7
DC20230523cell13	DC20230523cell14	8.9	0.7	7.5	3.8	8.9	55.1	3.2	12.0
DC20230621cell23	DC20230621cell24	8.7	0.6	7.2	3.8	8.2	56.7	3.2	11.6
DC20230523cell8	DC20230523cell9	1.7	11.1	0.4	6.3	12.2	38.7	5.9	23.7
DC20230713cell1	DC20230713cell2	8.9	5.5	15.5	1.3	27.8	9.9	3.1	32.0
DC20230713cell3	DC20230713cell4	0.7	6.7	9.6	12.6	9.5	19.3	3.4	38.2
DC20230713cell5	DC20230713cell6	9.5	17.6	1.3	2.1	9.8	30.2	9.8	19.6
DC20230713cell7	DC20230713cell8	9.0	0.7	10.1	6.9	9.5	41.3	9.9	12.7
DC20230713cell9	DC20230713cell10	17.9	8.6	2.5	7.2	30.2	10.2	16.9	6.5
DC20230713cell11	DC20230713cell12	1.9	5.1	10.1	7.5	26.5	28.2	3.0	17.7
DC20230713cell13	DC20230713cell14	13.4	2.0	10.7	4.9	27.9	9.9	6.2	24.9
DC20230713cell15	DC20230713cell16	7.5	6.9	13.5	2.5	17.6	37.5	8.8	5.6
DC20230714cell1	DC20230714cell2	10.5	1.3	6.8	3.1	54.1	9.4	3.0	11.9
DC20230714cell3	DC20230714cell4	3.0	7.0	19.1	2.4	20.9	22.3	18.1	7.2
DC20230714cell5	DC20230714cell6	1.1	7.8	16.0	14.1	11.9	12.6	28.4	8.0
DC20230714cell7	DC20230714cell8	11.7	2.5	3.3	16.1	0.0	12.1	15.7	38.5
DC20230714cell9	DC20230714cell10	2.6	15.8	6.8	0.8	28.1	18.6	3.2	24.1
DC20230714cell11	DC20230714cell12	22.2	1.9	2.6	0.9	46.0	0.0	19.2	7.2
DC20230714cell13	DC20230714cell14	2.2	5.1	7.3	5.6	56.2	47.7	0.0	0.0
DC20230714cell15	DC20230714cell16	6.6	1.7	18.3	9.9	68.0	0.0	0.0	29.3

DOSING RESUME TABLE

NAME_1	NAME_2	DOS_1	DOS_2	DOS	std_DOS
DC20230519cell1	DC20230519cell2	59.0%	61.0%	60.0%	1.4
DC20230621cell1	DC20230621cell2	57.0%	58.0%	57.5%	0.7
DC20230519cell3	DC20230519cell4	59.0%	60.0%	59.5%	0.7
DC20230621cell3	DC20230621cell4	60.0%	57.0%	58.5%	2.1
DC20230519cell5	DC20230519cell6	63.0%	58.0%	60.5%	3.5
DC20230621cell5	DC20230621cell6	56.0%	56.0%	56.0%	0.0
DC20230519cell7		56.0%	NaN	56.0%	
DC20230621cell7	DC20230621cell8	60.0%	60.0%	60.0%	0.0
DC20230519cell9	DC20230519cell10	61.0%	60.0%	60.5%	0.7
DC20230621cell9	DC20230621cell10	59.0%	58.0%	58.5%	0.7
DC20230519cell11	DC20230519cell12	58.0%	55.0%	56.5%	2.1
DC20230621cell11	DC20230621cell12	59.0%	58.0%	58.5%	0.7
DC20230523cell1	DC20230523cell2	60.0%	NaN	60.0%	
DC20230621cell13	DC20230621cell14	58.0%	69.0%	58.0%	
DC20230523cell3	DC20230523cell4	60.0%	63.0%	61.5%	2.1
DC20230621cell15	DC20230621cell16	59.0%	59.0%	59.0%	
DC20230523cell5	DC20230523cell6	63.0%	64.0%	63.5%	0.7
DC20230621cell17	DC20230621cell18	54.0%	57.0%	55.5%	2.1
DC20230523cell7		60.0%	NaN	60.0%	
DC20230621cell19	DC20230621cell20	59.0%	56.0%	57.5%	2.1
DC20230523cell11	DC20230523cell12	62.0%	67.0%	64.5%	3.5
DC20230621cell21	DC20230621cell22	59.0%	58.0%	58.5%	0.7
DC20230523cell13	DC20230523cell14	64.0%	NaN	64.0%	
DC20230621cell23	DC20230621cell24	58.0%	59.0%	58.5%	0.7
DC20230523cell8	DC20230523cell9	63.0%	64.0%	63.3%	0.6
DC20230713cell1	DC20230713cell2	59.6%	60.2%	59.9%	0.0
DC20230713cell3	DC20230713cell4	58.6%	61.9%	60.3%	0.0
DC20230713cell5	DC20230713cell6	60.6%	61.1%	60.9%	0.0
DC20230713cell7	DC20230713cell8	60.3%	59.1%	59.7%	0.0
DC20230713cell9	DC20230713cell10	60.4%	60.4%	60.4%	0.0
DC20230713cell11	DC20230713cell12	59.8%	60.1%	59.9%	0.0
DC20230713cell13	DC20230713cell14	59.8%	60.3%	60.1%	0.0
DC20230713cell15	DC20230713cell16	58.7%	59.4%	59.1%	0.0
DC20230714cell1	DC20230714cell2	59.5%	60.8%	60.2%	0.0
DC20230714cell3	DC20230714cell4	60.5%	57.6%	59.1%	0.0
DC20230714cell5	DC20230714cell6	62.6%	61.8%	62.2%	0.0
DC20230714cell7	DC20230714cell8	60.5%	60.3%	60.4%	0.0
DC20230714cell9	DC20230714cell10	61.3%	62.4%	61.8%	0.0
DC20230714cell11	DC20230714cell12	59.7%	60.0%	59.8%	0.0
DC20230714cell13	DC20230714cell14	62.4%	61.2%	61.8%	0.0
DC20230714cell15	DC20230714cell16	60.7%	62.2%	61.4%	0.0

PERFORMACES TABLE

NAME_1	NAME_2	CAP_1	CAP_2	CAP	std_CAP
DC20230519cell1	DC20230519cell2	6.1	2.1	4.1	2.8
DC20230621cell1	DC20230621cell2	4.7	4.8	4.7	0.1
DC20230519cell3	DC20230519cell4	174.9	146.6	160.7	19.9
DC20230621cell3	DC20230621cell4	141.7	158.5	150.1	11.9
DC20230519cell5	DC20230519cell6	54.1	70.4	62.2	11.5
DC20230621cell5	DC20230621cell6	76.2	64.0	70.1	8.7
DC20230519cell7		72.0	NaN	72.0	
DC20230621cell7	DC20230621cell8	51.9	52.8	52.4	
DC20230519cell9	DC20230519cell10	10.5	11.5	11.0	0.7
DC20230621cell9	DC20230621cell10	10.0	22.5	16.3	8.8
DC20230519cell11	DC20230519cell12	124.7	133.2	128.9	6.0
DC20230621cell11	DC20230621cell12	99.6	99.5	99.6	0.1
DC20230523cell1	DC20230523cell2	56.3	NaN	56.3	
DC20230621cell13	DC20230621cell14	48.6	21.3	48.6	
DC20230523cell3	DC20230523cell4	128.1	120.1	124.1	5.7
DC20230621cell15	DC20230621cell16	128.5	133.9	131.2	
DC20230523cell5	DC20230523cell6	81.4	111.2	96.3	21.1
DC20230621cell17	DC20230621cell18	113.2	80.2	96.7	23.3
DC20230523cell7		0.1	NaN	0.1	
DC20230621cell19	DC20230621cell20	3.8	3.8	3.8	0.0
DC20230523cell11	DC20230523cell12	1.4	0.8	1.1	0.4
DC20230621cell21	DC20230621cell22	4.3	4.9	4.6	0.4
DC20230523cell13	DC20230523cell14	111.1	NaN	111.1	
DC20230621cell23	DC20230621cell24	137.0	136.0	136.5	0.7
DC20230523cell8	DC20230523cell9	24.6	9.0	15.1	8.3
DC20230713cell1	DC20230713cell2	96.0	113.4	104.7	12.3
DC20230713cell3	DC20230713cell4	41.1	NaN	41.1	
DC20230713cell5	DC20230713cell6	NaN	3.0	3.0	
DC20230713cell7	DC20230713cell8	105.5	106.7	106.1	0.9
DC20230713cell9	DC20230713cell10	0.5	0.1	0.3	0.3
DC20230713cell11	DC20230713cell12	100.3	NaN	100.3	
DC20230713cell13	DC20230713cell14	72.0	116.7	94.3	31.6
DC20230713cell15	DC20230713cell16	67.6	101.2	84.4	23.8
DC20230714cell1	DC20230714cell2	128.7	128.0	128.4	0.4
DC20230714cell3	DC20230714cell4	64.1	75.9	70.0	8.3
DC20230714cell5	DC20230714cell6	12.1	14.5	13.3	1.7
DC20230714cell7	DC20230714cell8	8.9	12.0	10.4	2.2
DC20230714cell9	DC20230714cell10	1.8	2.3	2.0	0.3
DC20230714cell11	DC20230714cell12	94.9	98.8	96.9	2.7
DC20230714cell13	DC20230714cell14	120.0	140.3	130.1	14.3
DC20230714cell15	DC20230714cell16	55.0	55.1	55.0	0.1

7

APPENDIX-B

7.1 Models comparison

DoE – Regression model comparison

Linear Regression

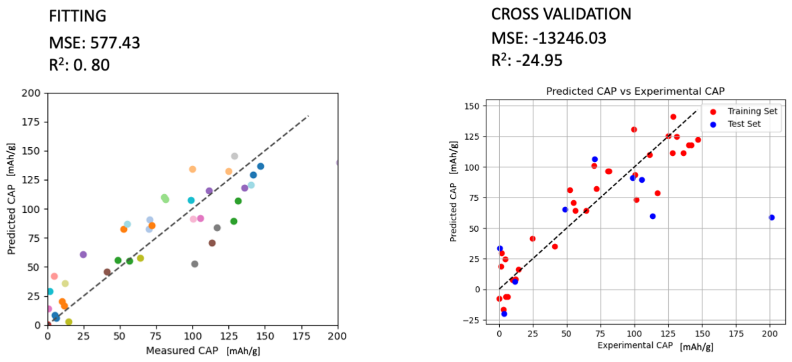
FITTING

MSE: 577.43

R^2: 0. 80

CROSS VALIDATION

MSE: -13246.03

R^2: -24.95

Figure 7.1: Comparison between the predicted capacity and the measured for Linear regression. Fitting (Left) using all the points for training and the same points for testing. Cross Validation (Right) 5 fold, 4 of them used for the training and the last one for the testing. Are also reported the values of MSE (mean squared error) and R^2

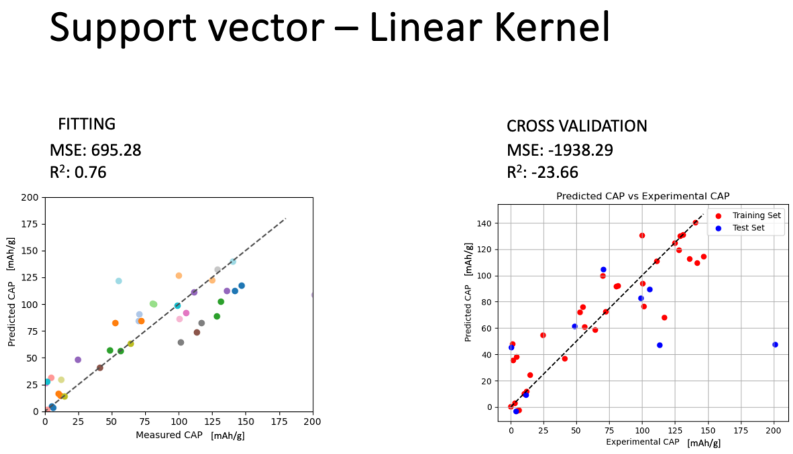

Support vector – Linear Kernel

FITTING

MSE: 695.28

R²: 0.76

CROSS VALIDATION

MSE: -1938.29

R²: -23.66

Figure 7.2: Comparison between the predicted capacity and the measured for support vector regression with linear kernel. Fitting (Left) using all the points for training and the same points for testing. Cross Validation (Right) 5 fold, 4 of them used for the training and the last one for the testing. Are also reported the values of MSE and R^2

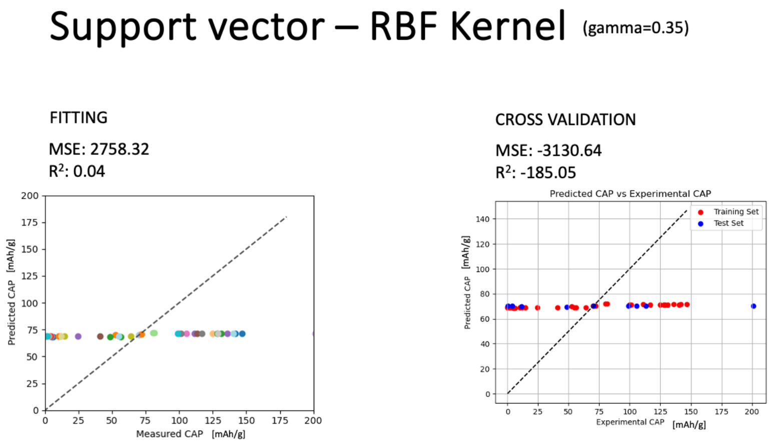

Support vector – RBF Kernel (gamma=0.35)

FITTING

MSE: 2758.32

R²: 0.04

CROSS VALIDATION

MSE: -3130.64

R²: -185.05

Figure 7.3: Comparison between the predicted capacity and the measured for support vector regression with Radial basis function kernel. Fitting (Left) using all the points for training and the same points for testing. Cross Validation (Right) 5 fold, 4 of them used for the training and the last one for the testing. Are also reported the values of MSE and R^2

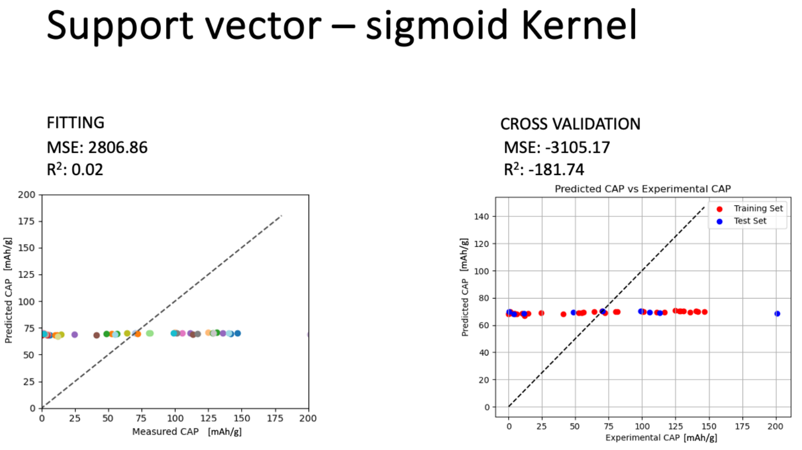

Support vector – sigmoid Kernel

FITTING
MSE: 2806.86
R^2: 0.02

CROSS VALIDATION
MSE: -3105.17
R^2: -181.74

Figure 7.4: Comparison between the predicted capacity and the measured for support vector regression with Sigmoid kernel. Fitting (Left) using all the points for training and the same points for testing. Cross Validation (Right) 5 fold, 4 of them used for the training and the last one for the testing. Are also reported the values of MSE and R^2

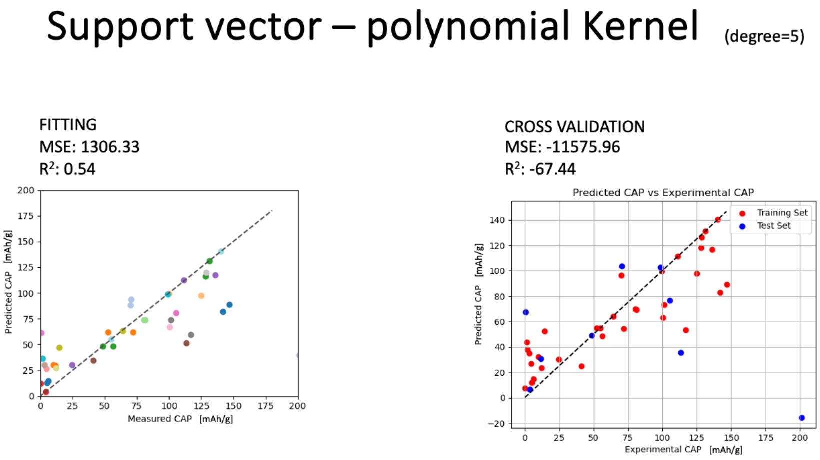

Support vector – polynomial Kernel (degree=5)

FITTING
MSE: 1306.33
R^2: 0.54

CROSS VALIDATION
MSE: -11575.96
R^2: -67.44

Figure 7.5: Comparison between the predicted capacity and the measured for support vector regression with Polynomial kernel with 5 degree of freedom. Fitting (Left) using all the points for training and the same points for testing. Cross Validation (Right) 5 fold, 4 of them used for the training and the last one for the testing. Are also reported the values of MSE and R^2

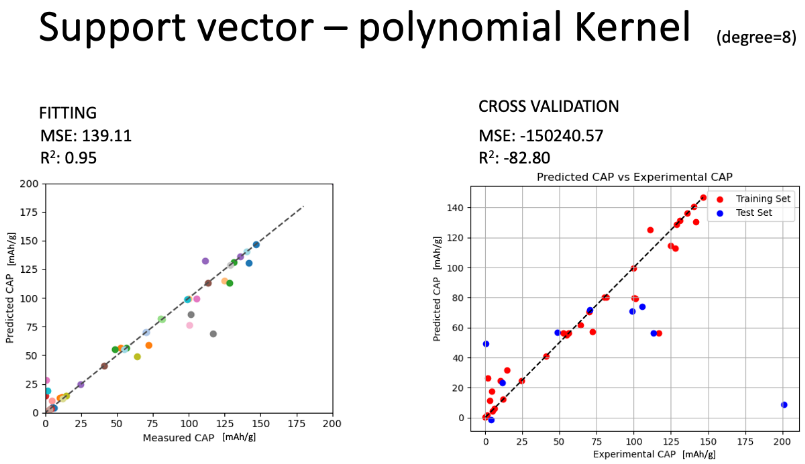

Figure 7.6: Comparison between the predicted capacity and the measured for support vector regression with Polynomial kernel with 8 degree of freedom. Fitting (Left) using all the points for training and the same points for testing. Cross Validation (Right) 5 fold, 4 of them used for the training and the last one for the testing. Are also reported the values of MSE and R^2

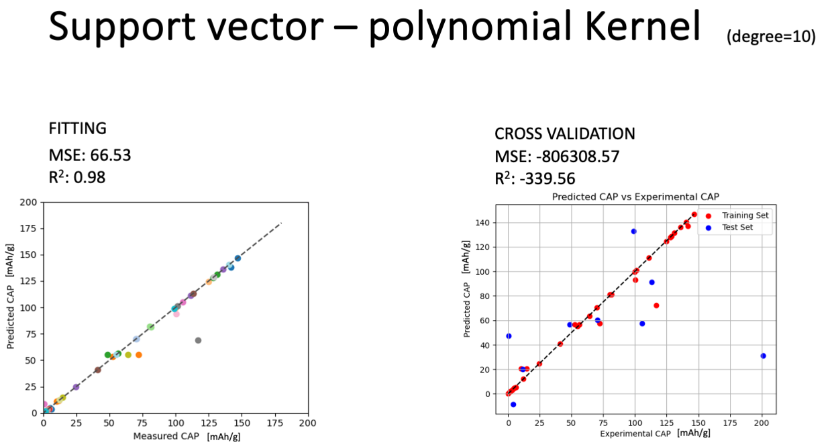

Figure 7.7: Comparison between the predicted capacity and the measured for support vector regression with Polynomial kernel with 10 degree of freedom. Fitting (Left) using all the points for training and the same points for testing. Cross Validation (Right) 5 fold, 4 of them used for the training and the last one for the testing. Are also reported the values of MSE and R^2

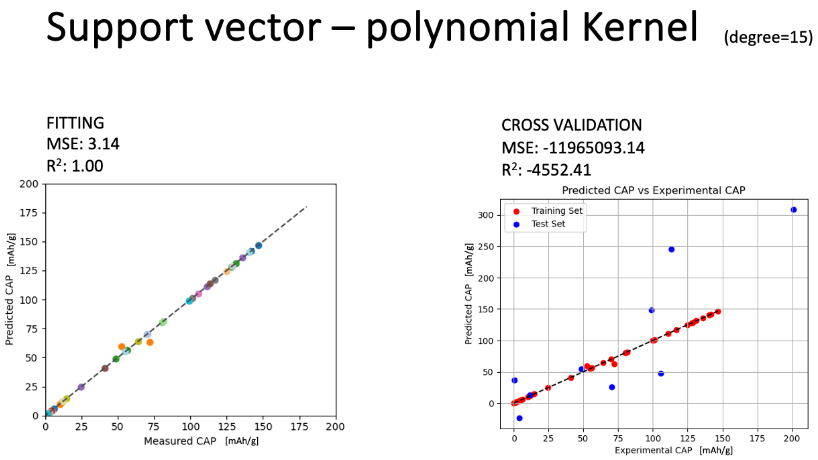

Figure 7.8: Comparison between the predicted capacity and the measured for support vector regression with Polynomial kernel with 15 degree of freedom. Fitting (Left) using all the points for training and the same points for testing. Cross Validation (Right) 5 fold, 4 of them used for the training and the last one for the testing. Are also reported the values of MSE and R^2

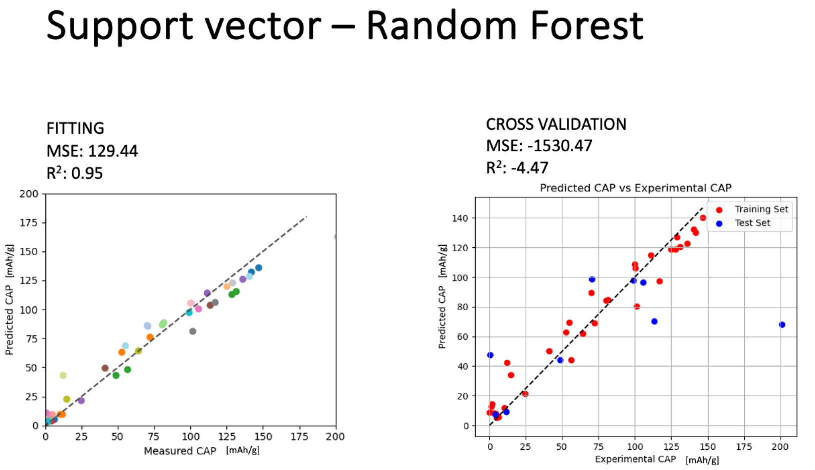

Figure 7.9: Comparison between the predicted capacity and the measured for Random forest regressor. Fitting (Left) using all the points for training and the same points for testing. Cross Validation (Right) 5 fold, 4 of them used for the training and the last one for the testing. Are also reported the values of MSE and R^2

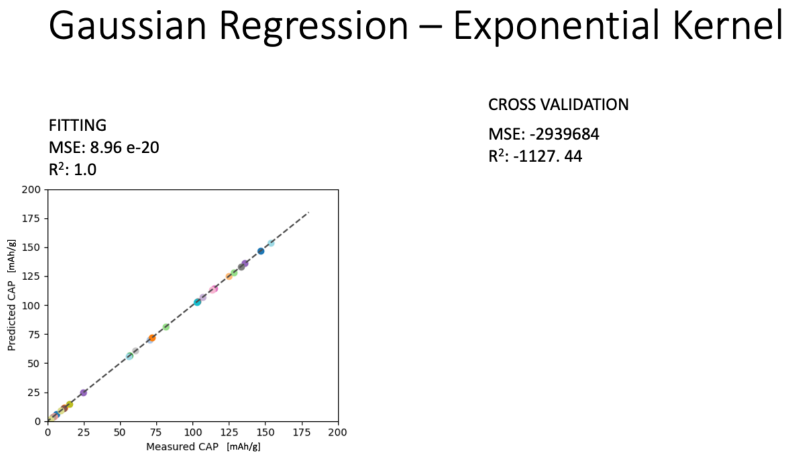

Figure 7.10: Comparison between the predicted capacity and the measured for Gaussian regression with exponential kernel. Fitting (Left) using all the points for training and the same points for testing. Cross Validation (Right) 5 fold, 4 of them used for the training and the last one for the testing. Are also reported the values of MSE and R^2

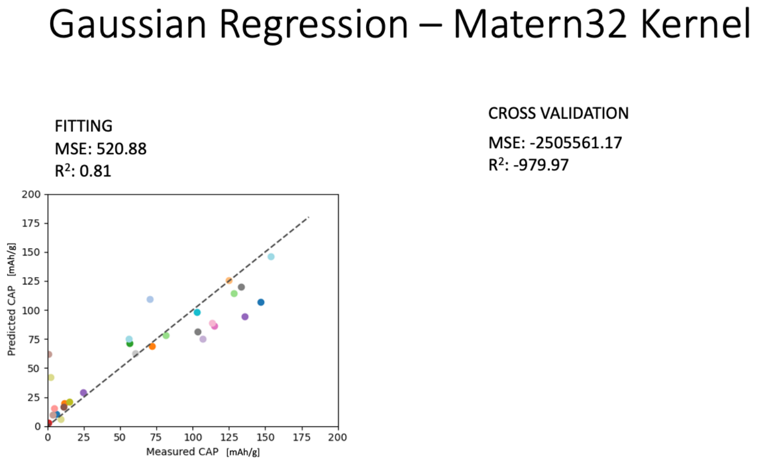

Figure 7.11: Comparison between the predicted capacity and the measured for Gaussian regression with Matern32 kernel. Fitting (Left) using all the points for training and the same points for testing. Cross Validation (Right) 5 fold, 4 of them used for the training and the last one for the testing. Are also reported the values of MSE and R^2

7.2 HOT ENCODED TABLE

Table 7.1: Hot-Encoded table, for different combinations of variable and capacity.

LiTFSI	LiBOB	LiCl	LiNO3	DOL	EC	G4	DMI	R^2
0	1	1	1	1	0	1	1	0.932372
1	1	0	0	1	1	1	1	0.929281
1	1	0	0	0	0	1	1	0.927195
0	1	0	0	0	1	1	1	0.927087
1	1	1	1	0	0	1	1	0.925873
0	1	1	1	1	0	1	0	0.92541
1	1	0	1	1	1	1	0	0.92397
1	1	1	1	0	1	1	0	0.923966
0	1	0	0	0	0	1	1	0.923524
0	1	0	1	1	1	1	0	0.923027
0	1	1	1	0	0	0	0	0.922792
0	1	1	1	1	1	1	1	0.922513
1	1	0	1	1	1	1	1	0.922269
0	1	0	1	0	1	1	1	0.922018
1	1	0	1	0	1	1	1	0.921892
1	1	0	1	0	1	1	0	0.921491
1	1	0	1	0	0	1	1	0.920935
0	1	0	1	0	0	1	1	0.920446
0	1	1	0	0	1	1	1	0.919545
0	1	0	0	1	1	0	1	0.919534
1	1	1	1	1	0	1	1	0.919359
0	1	1	1	0	0	1	1	0.919126
0	1	1	1	0	0	1	0	0.918788
1	1	0	1	0	0	1	0	0.9187
0	1	1	0	0	0	1	1	0.918069
0	1	0	0	1	0	1	1	0.917998
0	1	1	0	0	1	1	0	0.917942
1	1	1	1	1	0	1	0	0.917304
0	0	1	0	0	0	1	1	0.916919
1	1	1	1	1	1	0	0	0.916815
0	0	0	0	0	0	1	1	0.916236
0	1	0	1	1	0	0	0	0.915999
0	1	0	1	0	0	1	0	0.915899
0	1	0	1	1	0	0	1	0.915828
1	1	0	1	1	1	0	1	0.915685
0	1	1	1	1	1	1	0	0.914765
0	1	0	0	1	0	0	0	0.914516
1	1	0	1	1	0	0	0	0.914479

LiTFSI	LiBOB	LiCl	LiNO3	DOL	EC	G4	DMI	R^2
1	1	0	1	1	0	1	0	0.914
0	1	1	1	0	1	0	0	0.913698
1	1	1	0	1	1	0	1	0.913463
1	1	1	1	1	1	0	1	0.913306
1	1	0	0	0	1	1	1	0.91302
0	1	0	0	1	1	1	1	0.912699
1	1	1	0	0	1	1	1	0.912109
0	1	0	1	1	1	1	1	0.912027
0	1	0	1	1	0	1	1	0.911744
0	1	0	0	1	1	1	0	0.911732
0	1	1	1	0	1	1	1	0.911667
1	1	1	0	0	0	0	1	0.911528
0	0	1	0	0	1	1	1	0.911382
0	0	1	1	0	1	1	1	0.9111
0	1	1	0	1	0	0	1	0.91094
0	1	1	1	0	1	0	1	0.910832
0	1	1	0	1	0	1	0	0.910619
0	1	0	1	0	0	0	1	0.910466
1	1	0	0	1	0	1	1	0.910281
1	0	1	0	0	0	1	1	0.909766
1	1	1	0	1	0	1	1	0.909512
1	1	1	1	0	1	1	1	0.909459
1	1	0	0	0	1	1	0	0.909366
0	1	1	0	1	0	0	0	0.909302
0	1	0	1	0	1	0	1	0.909287
0	0	0	1	0	1	1	1	0.90926
0	1	0	1	0	1	0	0	0.909247
0	1	0	0	1	0	0	1	0.909036
1	1	0	0	1	1	0	1	0.909024
0	1	0	0	0	0	0	1	0.90878
0	1	1	0	1	1	1	1	0.908735
0	1	1	0	1	1	1	0	0.908539
0	1	0	1	1	0	1	0	0.908523
1	1	0	1	1	1	0	0	0.908326
1	1	1	0	1	0	1	0	0.908309
0	1	1	1	1	0	0	0	0.90797
0	1	0	1	0	1	0	1	0.907935
1	1	0	0	1	0	0	1	0.90782
0	1	0	0	0	1	1	0	0.9075

LiTFSI	LiBOB	LiCl	LiNO3	DOL	EC	G4	DMI	R^2
0	1	0	0	1	1	0	0	0.907191
0	1	0	0	1	0	1	0	0.907149
0	1	1	1	1	1	0	0	0.907059
1	1	0	0	1	1	0	0	0.906836
0	1	1	0	0	0	1	0	0.906681
1	0	0	1	1	1	1	1	0.906680
1	1	1	1	1	0	0	0	0.906572
1	1	1	1	1	1	1	0	0.906456
1	1	0	1	1	0	0	1	0.906086
1	1	1	0	1	0	0	0	0.905409
1	1	0	1	1	0	1	1	0.905233
0	1	0	1	0	0	0	0	0.905139
1	1	1	1	0	0	1	0	0.905117
1	1	1	0	0	0	1	1	0.904844
1	1	1	0	1	1	0	0	0.904391
0	1	0	0	0	1	0	1	0.904316
1	1	1	0	0	0	1	0	0.904210
1	1	1	1	0	0	0	1	0.904106
1	1	1	1	0	1	0	0	0.903795
0	1	0	1	1	1	0	0	0.903507
1	1	0	0	1	0	0	1	0.903327
0	1	0	1	1	1	0	1	0.903245
0	1	1	0	1	1	0	1	0.903182
1	1	1	1	1	0	0	1	0.903132
1	0	0	1	0	0	1	1	0.902721
1	0	0	0	1	1	1	1	0.902698
1	1	1	0	1	1	1	1	0.902662
1	1	1	1	1	1	1	1	0.902068
0	1	0	0	0	0	1	0	0.902066
1	1	1	1	0	0	0	0	0.901931
0	1	1	1	0	1	1	0	0.901454
1	1	0	0	1	1	1	0	0.901434
1	0	1	1	0	1	1	1	0.900504
0	1	1	1	0	0	0	1	0.900486
1	0	0	0	1	1	0	1	0.899949
1	0	1	1	1	1	1	1	0.899129
1	0	0	0	1	0	1	1	0.899054
1	0	0	1	1	1	1	0	0.898860
0	0	1	0	1	1	0	1	0.898693

LiTFSI	LiBOB	LiCl	LiNO3	DOL	EC	G4	DMI	R^2
1	1	0	1	0	0	0	1	0.898429
0	0	1	0	0	0	0	1	0.898269
1	1	0	0	0	1	1	0	0.897859
1	1	0	1	0	0	0	0	0.897478
0	1	1	0	0	0	0	1	0.897379
1	0	1	0	0	1	1	1	0.897354
1	0	1	0	0	1	1	1	0.897354
0	0	0	0	0	1	1	1	0.897166
1	1	1	0	1	1	1	0	0.896938
0	1	1	1	1	1	0	1	0.896649
1	0	1	1	1	0	1	1	0.896553
1	0	0	0	1	1	1	0	0.896514
1	0	0	1	0	1	1	1	0.895286
0	0	1	0	1	1	0	1	0.895222
0	1	1	1	1	0	0	1	0.895215
1	0	0	1	1	0	1	1	0.895193
0	1	1	0	0	1	0	1	0.895020
1	1	0	1	0	0	0	1	0.894897
0	0	1	0	1	1	1	1	0.894816
1	1	0	1	0	1	0	1	0.894552
0	1	1	0	1	1	0	0	0.894544
0	0	0	0	1	0	1	1	0.894462
1	1	1	0	1	0	0	1	0.894443
0	0	1	1	0	0	1	1	0.894321
1	1	1	0	0	1	1	0	0.894287
0	0	1	0	0	1	0	1	0.893818
1	0	1	0	1	0	0	1	0.893120
1	1	0	0	0	0	1	0	0.892813
1	0	0	0	0	0	1	0	0.892265
0	1	1	0	0	0	0	0	0.892160
1	0	1	1	0	1	0	1	0.892086
1	1	0	0	0	1	0	1	0.892010
1	0	1	0	1	1	0	0	0.891771
1	0	1	1	1	0	0	1	0.891761
1	0	1	0	1	1	1	0	0.891723
1	0	1	1	0	0	0	1	0.891190
1	0	1	0	1	0	1	1	0.891128
0	1	1	0	1	0	1	1	0.890865
1	0	1	1	1	1	1	0	0.890817

LiTFSI	LiBOB	LiCl	LiNO3	DOL	EC	G4	DMI	R^2
1	0	1	0	1	1	1	1	0.890642
0	0	0	0	1	1	0	0	0.890557
1	1	1	0	0	1	0	1	0.890446
1	0	1	0	1	0	1	0	0.890372
0	0	1	1	1	0	1	1	0.889720
0	0	1	0	1	0	1	1	0.889606
1	0	0	0	1	0	0	1	0.889385
0	1	0	0	0	1	0	0	0.889175
0	0	0	1	0	0	1	1	0.888929
1	1	1	1	0	1	0	1	0.888728
0	0	1	0	1	0	0	1	0.888215
1	0	0	0	1	1	0	0	0.888136
1	0	0	0	0	1	1	1	0.887927
0	1	0	0	0	0	0	0	0.886913
1	1	1	0	0	0	0	0	0.886427
1	0	1	1	1	1	0	1	0.886337
1	1	0	0	0	0	0	1	0.885665
1	0	0	0	1	0	1	0	0.885348
0	0	0	0	1	1	0	1	0.885330
0	1	1	0	0	1	0	0	0.884851
1	0	1	1	0	0	1	1	0.884820
0	0	0	1	1	1	1	1	0.883825
1	0	0	0	0	1	1	0	0.883163
0	0	0	0	0	1	1	0	0.883119
0	0	1	1	1	1	0	0	0.883076
0	0	1	1	1	1	1	1	0.883037
1	0	1	0	1	1	0	1	0.882645
0	0	1	1	0	0	0	1	0.882448
1	0	1	0	0	1	0	1	0.882445
0	0	0	1	1	1	0	0	0.882389
1	0	1	0	0	0	0	1	0.882203
0	0	0	1	1	1	0	1	0.882177
1	1	0	0	0	0	0	0	0.881984
0	0	0	1	1	0	1	1	0.881507
0	0	0	1	1	1	1	0	0.881499
1	0	0	1	1	1	0	1	0.881039
1	0	0	0	1	0	0	0	0.880835
1	0	0	1	1	0	1	0	0.880181
0	0	0	0	1	1	1	1	0.879473

LiTFSI	LiBOB	LiCl	LiNO3	DOL	EC	G4	DMI	R^2
0	0	1	0	1	0	1	0	0.879431
1	1	0	1	0	1	0	0	0.879152
1	0	0	1	1	0	1	0	0.878006
1	0	0	1	1	1	0	0	0.876164
0	0	1	1	1	0	1	0	0.875663
0	0	1	0	0	1	1	0	0.874435
1	1	0	0	0	1	0	0	0.874078
0	0	1	1	0	1	0	1	0.874006
0	0	1	0	1	1	1	0	0.873845
0	0	1	1	1	1	0	1	0.872753

8

APPENDIX-C

8.1 Experimental measures of cathode optimization

Initially, a set of experiments was conducted with a high dosing percentage (65%), and pronounced shuttling was observed. This could be attributed to the chloride concentration or the high iodine concentration, which facilitates dissolution.

Subsequently, the decision was made to decrease the dosing percentage to determine whether the shuttling issue was influenced by the absolute quantity of salts or the ratio between the salts and PVP. We compared three potential dosing solutions. The first solution included PVP, MADQUAT, and carbon black. The two polymers were intended to bind the two salts, while carbon black played a role in maintaining high conductance for efficient cycling. The other two dosing solutions did not contain MADQUAT and had slight composition variations. The results are presented in figure 8.1.

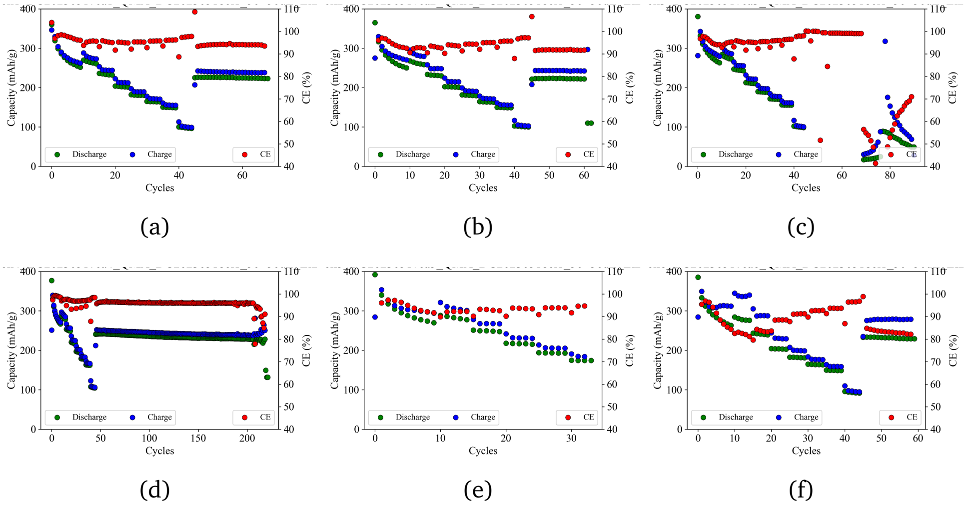

(a) (b) (c)

(d) (e) (f)

Figure 8.1: (a)-(b) Capacity during the standard cycle for the first dosing solution (c)-(d) Capacity during the standard cycle for the second solution (e)-(f) Capacity during the standard cycle for the third solution. Experiment for 40% dosing.

All the cells performed exceptionally well, demonstrating a superiority of the formulation without MADQUAT.

Subsequently, I decided to replicate the experiment to validate the observed trend and attempt to increase the PVP content. The internal resistance measured using EIS was relatively low, suggesting potential for increasing the binder mass. We are also monitoring the impact of the PVP on the $LiI/LiCl$ absorption, with SEM and characterization for different dosing mass and PVP concentration.

8.2 Solvent amount comparison

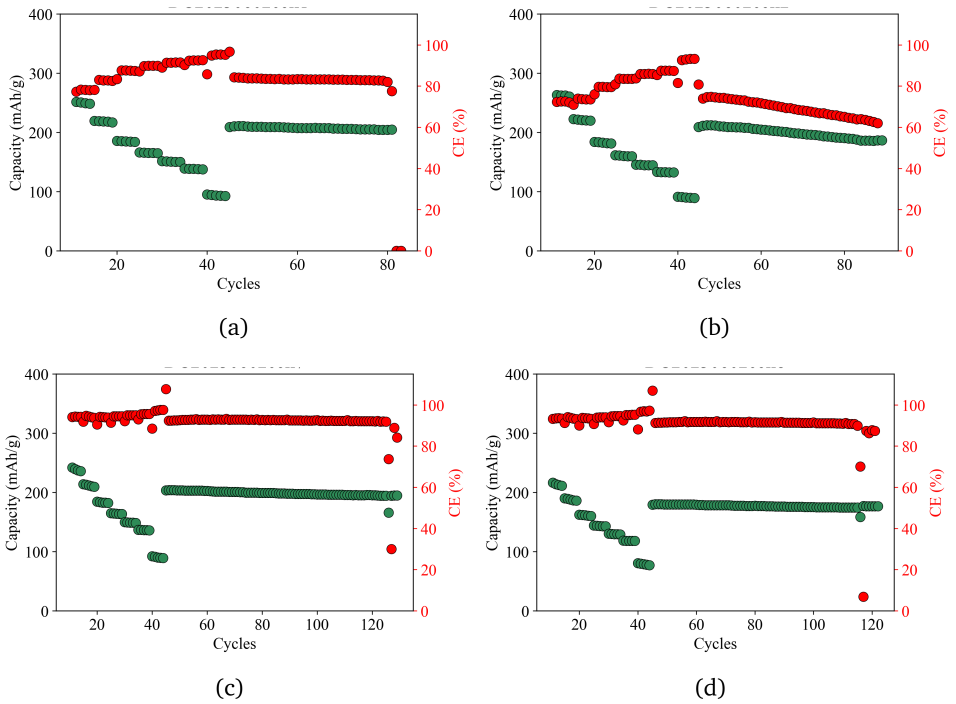

(a)

(b)

(c)

(d)

Figure 8.2: Comparison varying the quantity of solvent EtOH, (c-d) have double solvent quantity with respect to (a-b). Increase in the efficiency

8.3 PVP concentration comparison

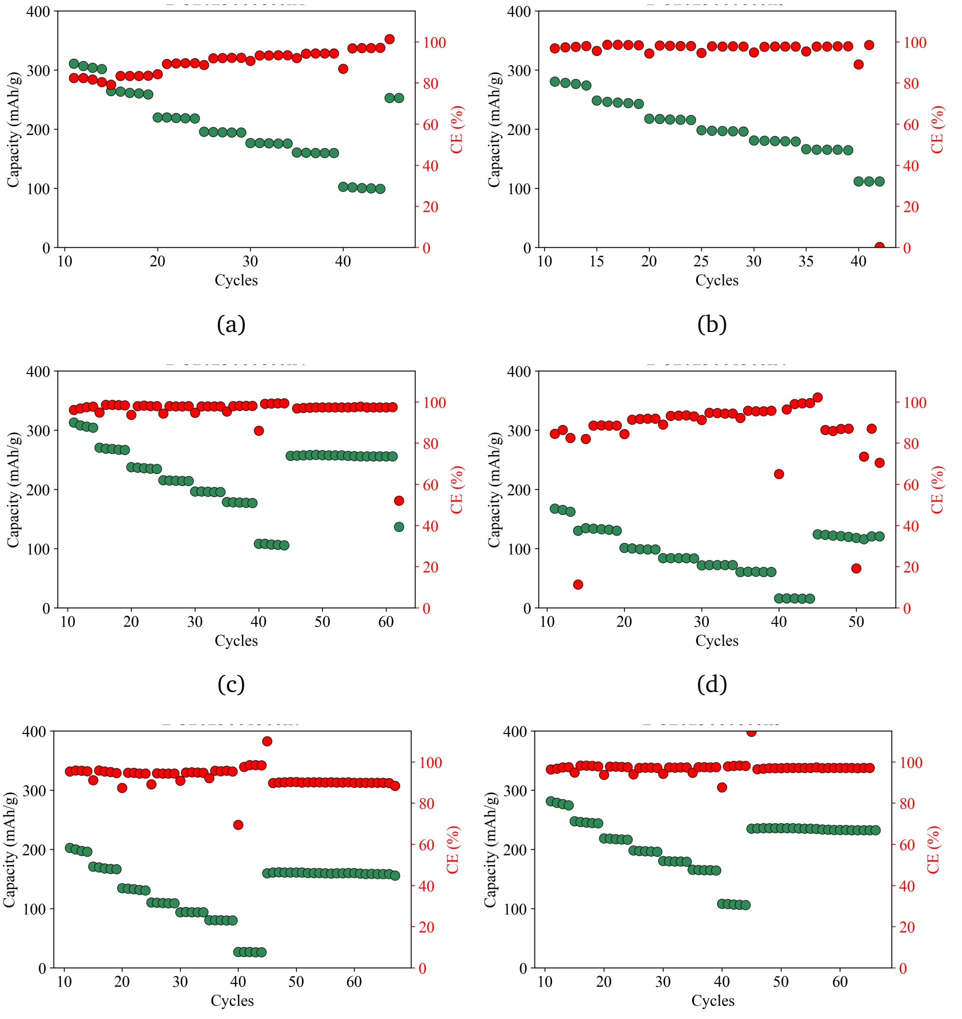

(a) (b)

(c) (d)

(e) (f)

Figure 8.3: Comparison varying the amount of binder, (a-b) low quantity of PVP, and target dosing 45%. (c-d) doubled quantity of PVP with respect of (a-b), (c) target dosing 45%, (d) target dosing 60%. (e) same quantity of (c-d) with increased KB and LiCl, (e) target dosing 45%. (f) doubled quantity of PVP with respect of (c-d), (f) target dosing 45%

8.4 PVP concentration comparison

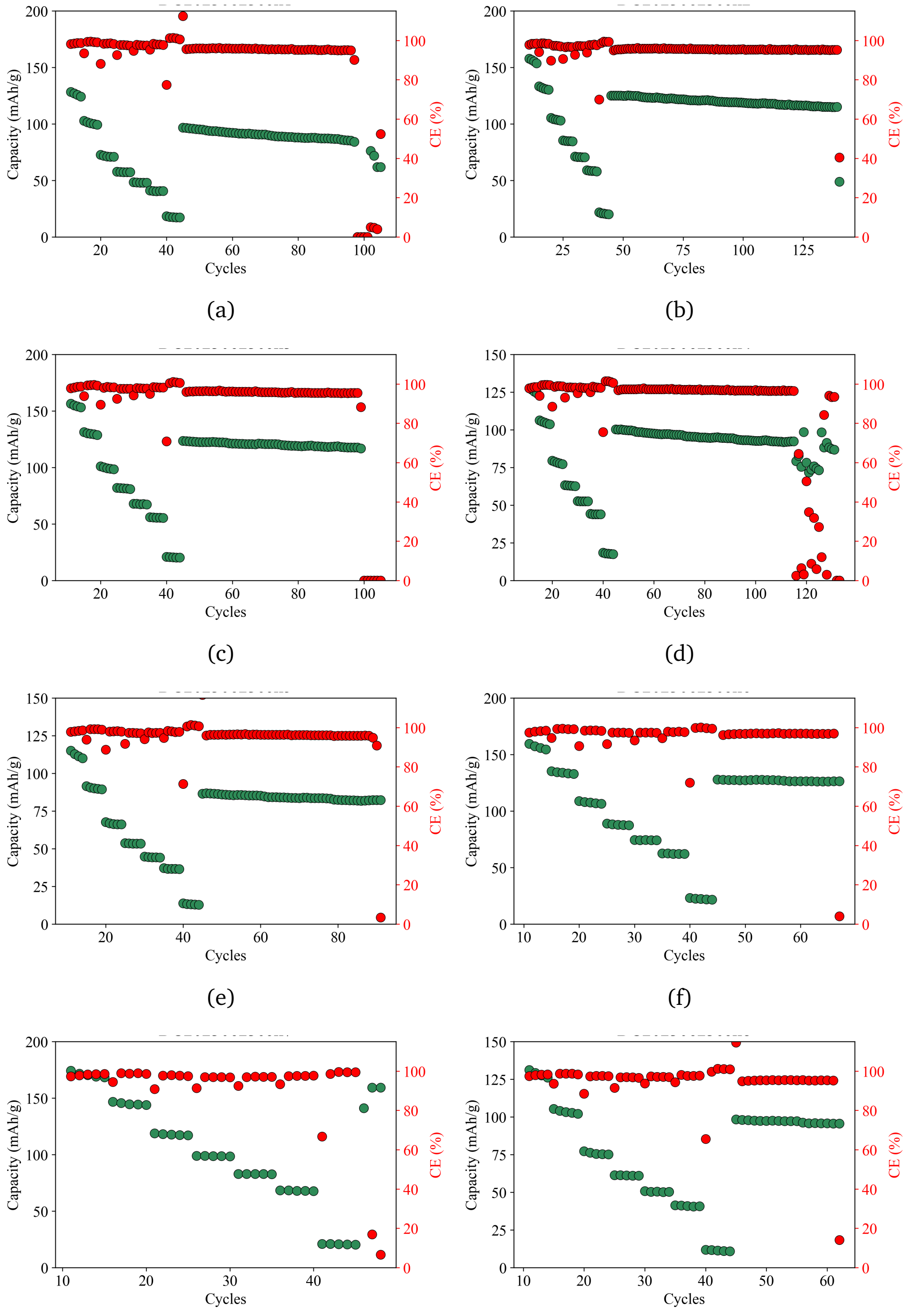

(a) (b) (c) (d) (e) (f) (g) (h)

Figure 8.4: Comparison varying the amount of binder, with 60% target dosing. (a-b) no PVP binder. (c-d) 4 mg of PVP binder. (e-f) 8 mg of PVP binder. (g-h) 16 mg of PVP binder.

8.5 PVP and MADQUAT comparison

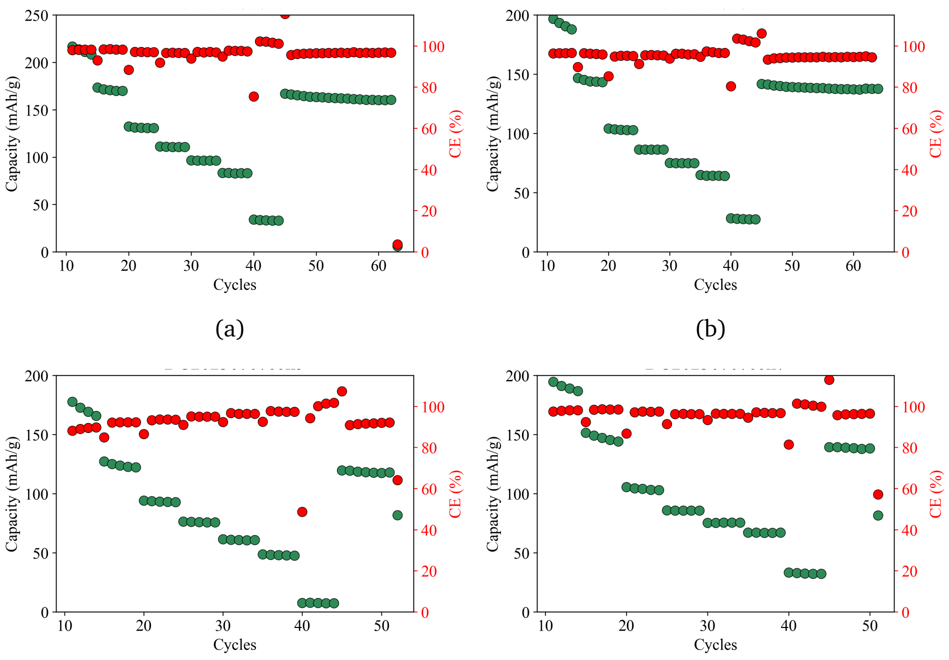

(a)

(b)

(c)

(d)

Figure 8.5: Comparison varying the amount of binder, with 60% target dosing. (a) PVP binder.(b) PVP and MADQUAT (1:1 wt.) binder.(c) MADQUAT binder.(d) no binder.

8.6 Increased dosing percentage

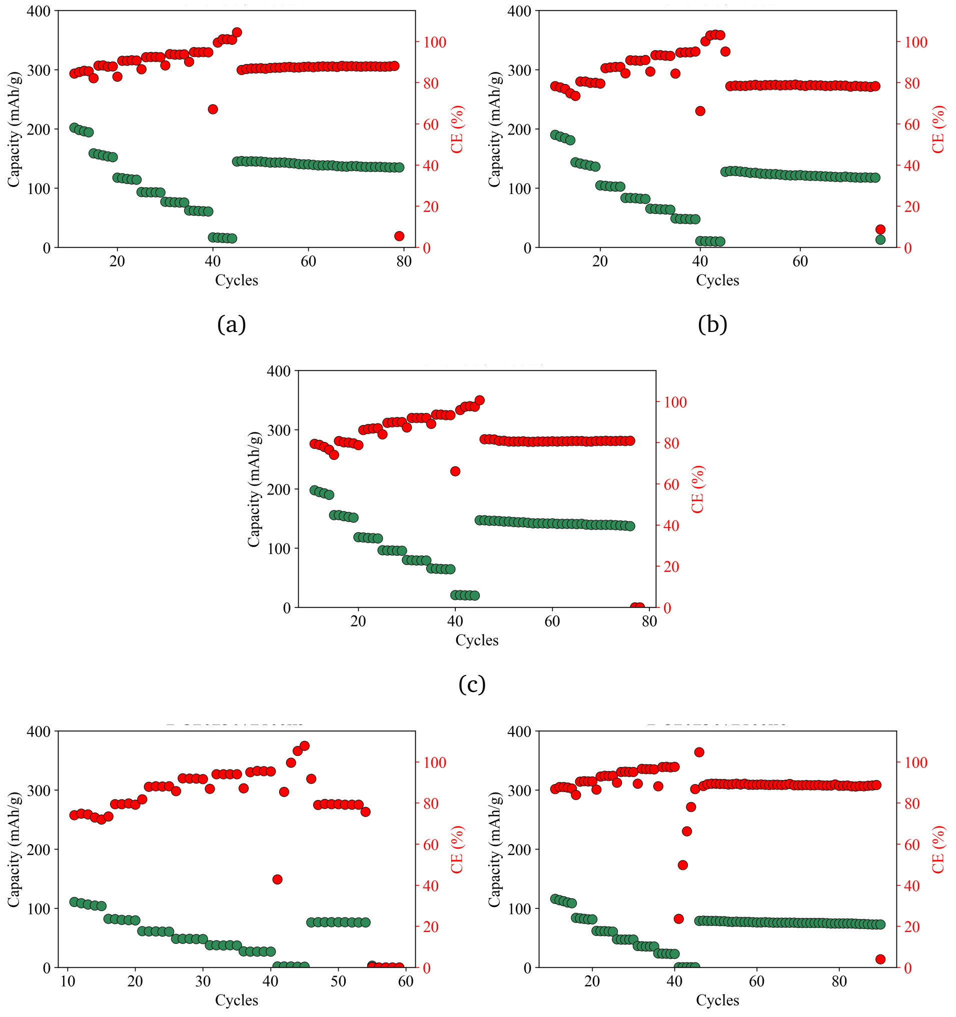

(a)

(b)

(c)

(d)

(e)

Figure 8.6: (a-b) target 60% dosing.(c) target 60% dosing, with increased LiCl. (d-e) target 70% dosing.

8.7 Integration and dissolution collaboration

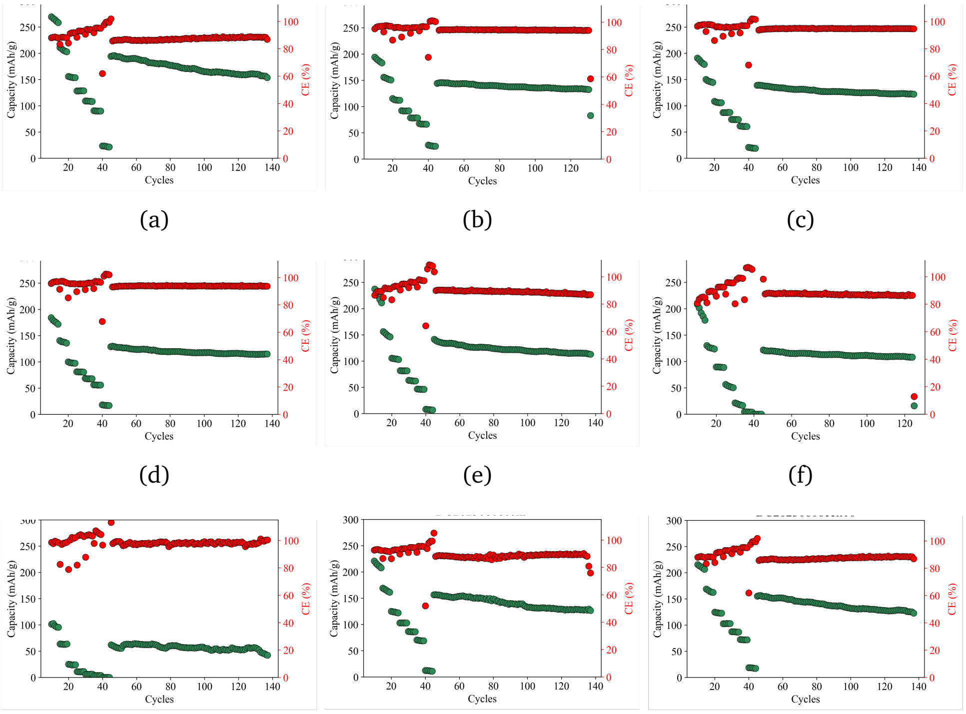

(a) (b) (c)

(d) (e) (f)

(g) (h) (i)

Figure 8.7: Comparison between LiCl just in the cathode or both in cathode and electrolyte, target dosing 60%. (a-b-c-d-e-f-g) no binder, (h-i) PVP and KB. (a-b-h-i) no LiCl in the electrolyte, (c-d) no LiCl in the electrolyte, with slightly different compositions. (e-f) LiCl in the electrolyte. (g) LiCl in the electrolyte, with slightly different compositions.